Acta Geochim (2025) 44:1014–1039
https://doi.org/10.1007/s11631-025-00800-y

ORIGINAL ARTICLE

Mineralogy, geochemistry, and stable isotopes in the reconstruction of the paleodepositional environment, provenance, and paleoclimate of Cretaceous mudstones, Koum Basin, Cameroon

Nowel Yinkfu Njamnsi[1,3] · George Lemewihbwen Ngiamte[2,3] · Cheo Emmanuel Suh[2,4] · Olivier Anoh Njoh[2] · Daniel Layton-Matthews[5] · Peir K. Pufahl[5] · Agatha Dobosz[5]

Received: 20 February 2025 / Revised: 22 May 2025 / Accepted: 4 June 2025 / Published online: 1 July 2025
© The Author(s), under exclusive licence to Science Press and Institute of Geochemistry, CAS and Springer-Verlag GmbH Germany, part of Springer Nature 2025

Abstract The Cretaceous Koum Basin is a rift-related half-graben in northern Cameroon, which constitutes a portion of the Yola Arm of the Upper Benue Trough. This study presents the first comprehensive dataset combining mineralogical, bulk-rock geochemical, and stable C–H–O isotopic data for dark-gray, fine-grained mudstones from the basin, providing new insights into its sediment source, paleoenvironment, and geodynamic setting. The mudstones primarily consist of phyllosilicates (~ 8.6%), feldspars (~ 30.5%), carbonates (~ 13.7%), and minor iron oxides (~ 2.7%), with vermiculite, illite, and kaolinite as the main clay minerals. The presence of analcime, ankerite, and dolomite suggests low-grade metamorphism and/or hydrothermal alteration. Fe_2O_3/K_2O (1.52–6.40) and SiO_2/Al_2O_3 (2.97–4.68) ratios classify the mudstones as compositionally immature shales (ICV ~ 1.64) with low-moderate chemical weathering (CIA ~ 56.35; PIA ~ 59.74; $R^{3+}/R^{3+} + R^{2+} + M^{+}$ ~ 0.51). Trace element ratios (Th/Sc ~ 1.70, Zr/Sc ~ 1.33, La/Sc ~ 6.30, La/Th ~ 4.14) indicate an intermediate igneous provenance from a continental crustal source. Paleoenvironmental proxies suggest deposition in a dynamic basin environment marked by fluctuating redox (C_{org}/P: 0.21–178.34) and salinity (Sr/Ba: 0.34–3.25; N-values: 48–35.92) conditions, ranging from oxic to anoxic and brackish to saline. Major element data (SiO_2 vs. $Al_2O_3 + K_2O + Na_2O$) indicate a semi-arid regime, while Paleoclimatic indicators such as Sr/Cu (1.88–37.47) and C-values (0.12–0.93) suggests alternating humid and arid conditions. Notably, stable isotope data, reported here for the first time in the Koum Basin, reveal a predominantly terrestrial, fluvial-deltaic C_3 plant source for organic carbon ($\delta^{13}C$ − 25.2‰ to − 35.2‰) and complex fluid-rock interactions involving meteoric and magmatic-metamorphic fluids under a warm, equatorial climate ($\delta^{18}O$ + 3.6‰ to + 24.9‰, $\delta^{2}H$ − 104‰ to − 50‰). The combined mineralogical, geochemical, and isotopic data point to deposition in a tectonically active continental arc setting, with contributions from ocean island arc and passive margin sources.

Keywords Geochemistry · C–H–O isotopes · Sediment source · Paleoenvironment · Paleoclimates · Koum basin

1 Introduction

The oil and gas industry is undergoing a significant transformation, driven by a global shift toward sustainability and a move away from fossil fuels. Despite growing environmental

Supplementary Information The online version contains supplementary material available at https://doi.org/10.1007/s11631-025-00800-y.

✉ George Lemewihbwen Ngiamte
ngiamte.george@yahoo.com

[1] Exploration Division, Department of Promotion State-owned Oil and Gas Assets, National Hydrocarbons Corporation (SNH), P.O. Box 955, Yaoundé, Centre Region, Cameroon

[2] Mineral Exploration Geoscience Program, Pan African University Life and Earth Sciences Institute (Including Health and Agriculture), P.M.B 20, Ibadan, Oyo State, Nigeria

[3] Department of Geology, Mining and Environmental Science, The University of Bamenda, P.O. Box 39, Bamenda, Northwest Region, Cameroon

[4] Economic Geology Unit, Department of Geology, University of Buea, P.O. Box 63, Buea, Southwest Region, Cameroon

[5] Queen's Facility for Isotope Research, Department of Geological Sciences and Geological Engineering, Queen's University, 36 Union Street, Kingston, ON K7L 3N6, Canada

concerns and uncertainties surrounding the long-term availability of hydrocarbon reserves, oil remains a crucial economic driver, particularly for developing nations (Graham and Ovadia 2019; Campbell and Heapes 2008; Höök et al. 2009; Di Muszio and Ovadia 2006; Ghasemian et al. 2020; Litvinenko 2020). This continued reliance on oil necessitates the identification of new hydrocarbon reserves to meet global energy demands, especially in data-scarce regions. Consequently, exploration efforts are increasingly targeting complex geological settings and frontier basins as production from mature fields declines (Lawson et al. 2018; Latham 2019).

Understanding past climatic and depositional environments is crucial for both hydrocarbon exploration and predicting future climate change. Paleoclimate research utilizes various proxies, including clay mineralogy (Ruffell and Batten 1990; Hallam et al. 1991; Ruffell and Garden 1997) and, importantly, stable isotope geochemistry, which has proven particularly valuable in reconstructing past environmental conditions and geochemical processes (McCrea 1950; Urey et al. 1951; Silverman and Epstein 1958; Boutton et al. 1993; Xie et al. 2000; Sauer et al. 2001; Dawson et al. 2004; Leng and Marshall 2004; Tiwari et al. 2015; Tabor and Myers 2015; Peng et al. 2024; Sofer 1991).

The Cretaceous Period, characterized by a greenhouse climate and various geological events (Tarduno et al. 1998; Kuypers et al. 1999; Cojan et al. 2000; Berner and Kothavala 2001; Bice and Norris 2002; Huber et al. 2002; Skelton et al. 2003; Bice et al. 2006), provides an excellent case study for investigating these relationships. Research on the paleodepositional and climatic conditions of Cretaceous rift basins is particularly relevant for understanding hydrocarbon formation and informing future climate models (Lentini et al. 2010; Chaboureau et al. 2013).

Rift basins globally, including those in West Siberia, Africa, South America, China, and Southeast Asia, are known for their significant hydrocarbon potential (Morley 1999; Harris et al. 2004). The West and Central African Rift System (WCARS) is a prime example. While its hydrocarbon potential has long been recognized, development has been hampered by infrastructure limitations. Recent advancements, such as the construction of the Chad–Cameroon pipeline, are now facilitating exploration and production activities in this region (Fairhead 2009; Dou et al. 2023).

While the Benue Trough, a major basin within the WCARS, has been extensively studied, significant hydrocarbon discoveries have been limited. However, the recent discovery in the Kolmani River Field by the Nigerian National Petroleum Company marks a significant milestone. Other promising basins within the WCARS include the East Niger and Sudanese rift basins, as well as basins in northern Cameroon, such as Logone Birni, Garoua, Yaogoua, Babouri Figuil, and Koum (Petters and Ekweozor 1982; Nwachukwu 1985; Genik 1992; Bessong et al. 2018; Njamnsi et al. 2022a, b).

The Koum basin, a Cretaceous rift basin in northern Cameroon, is a remnant of the Yola Arm of the Upper Benue Trough (Fig. 1). Located at the intersection of the Central African Rift System (CARS) and the West African Rift System (WARS), the basin has attracted considerable attention due to its exposed geological formations and potential for hydrocarbon resources. Numerous studies have investigated its structural, stratigraphic, and paleodepositional characteristics (e.g., Congleton 1990; Nolla et al. 2015; Shandini et al. 2018; Bessong et al. 2018; Njamnsi et al. 2022a, b; Agbor-Taku et al. 2023a, b, c; Ngo Mandeng et al. 2024a, b).

Recent studies have identified organic-rich mudstones with significant oil generation potential within the Koum basin (e.g., Njamnsi et al. 2022b; Ngo Mandeng et al. 2024a). These mudstones contain predominantly Type I-II kerogen, indicating oil-prone organic matter, along with some Type III kerogen associated with gas generation. The organic matter in these rocks is derived from a mixture of algal and terrestrial sources (Njamnsi et al. 2022a, b; Ngo Mandeng et al. 2024a, b). However, despite these advances, no study to date has provided a detailed, integrated mineralogical, whole-rock geochemical, and stable C–H–O isotopic characterization of the mudstones from the Koum Basin. This lack of comprehensive geochemical and isotopic data limits our understanding of the basin's sediment provenance, depositional environment, fluid interactions, and tectonic evolution critical factors for assessing its petroleum potential.

This study addresses this gap by presenting the first integrated dataset of mineralogical, major-trace element geochemistry, and stable C–H–O isotope compositions for the dark-gray Cretaceous mudstones of the Koum Basin. This combined approach provides novel insights into sediment provenance, paleoclimate variability, diagenetic processes, and the basin geodynamics. These findings not only advance the geological understanding of the Koum Basin but also contribute to broader regional exploration models and the economic development of northern Cameroon.

2 Geological setting

The Koum basin, a 1200-km^2 intracontinental basin in northern Cameroon, is an extension of the Yola sub-basin within the Upper Benue Trough of Nigeria (Fig. 1; Brunet et al. 1990; Maurin et al. 1986; Schwoerer 1965). As part of the WCARS, the formation and geometry of the Koum basin are linked to tectonic activity during the Early Cretaceous, specifically strike-slip or extensional tectonics along

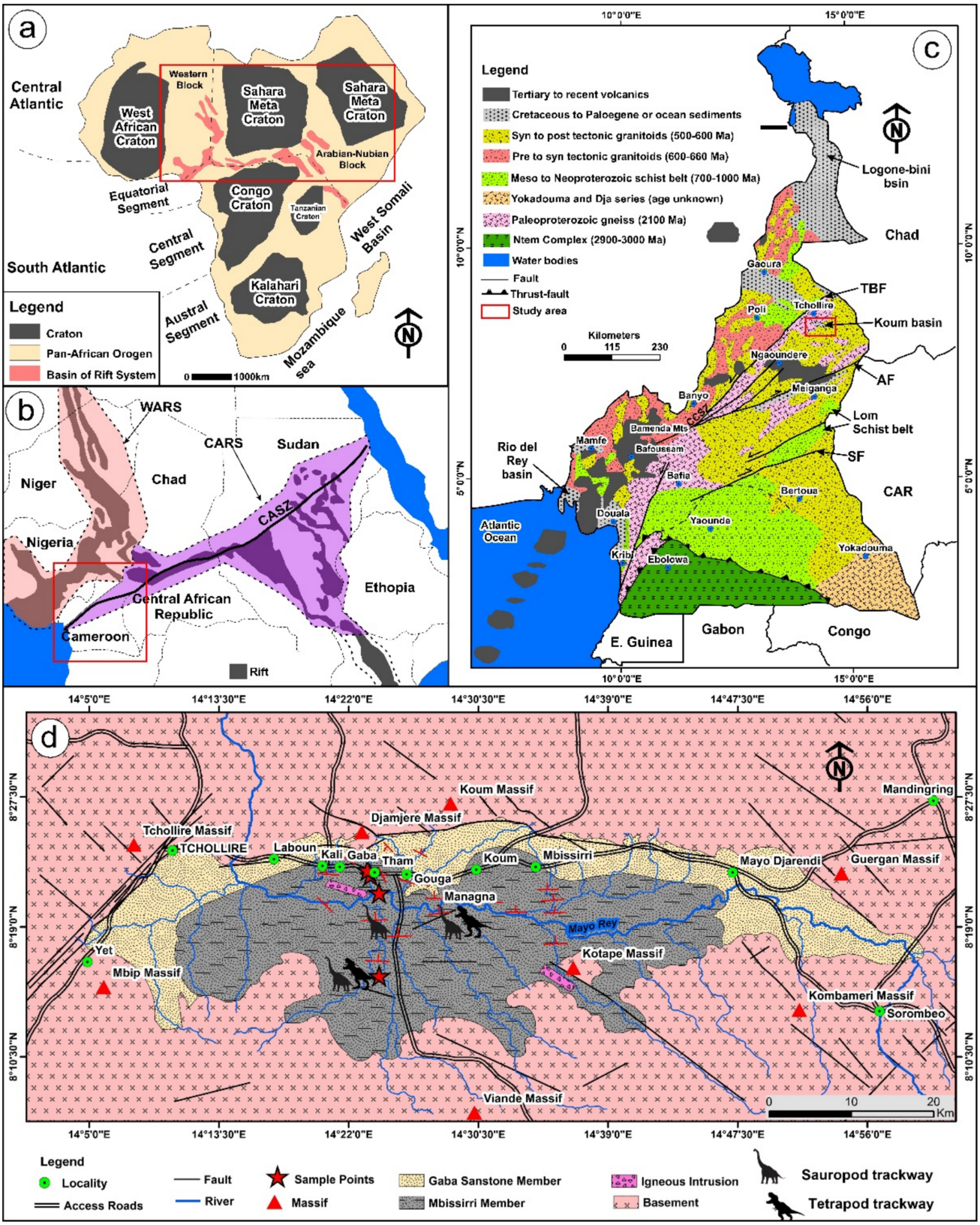

Fig. 1 Map illustrating **a**, **b** the configuration of the West and Central African Rift System (adapted from Genik 1993; Fairhead 2020), **c** the regional geologic setting of Cameroon, with the Koum basin indicated by the *red inset* (modified from Mimba et al. 2018), and **d** the specific geologic formations within the Koum basin (adapted after Congleton 1990; Jacobs et al. 1996; Njamnsi et al. 2022a)

reactivated Pan-African Mobile Belt structures (Fig. 1a, b; Mateer et al. 1992; Fairhead 2020).

The Koum basin is a half-graben structure filled with up to 4500 m of fluvio-lacustrine to intertidal sediments. The basin's asymmetrical shape, with a synclinal structure in the northwest and a homoclinal dip to the southeast, is primarily controlled by major synsedimentary faults, particularly along the northern margin of the basin (Fig. 1c). Three main structural trends characterize the Koum basin: NNW–SSE and E–W basin boundary faults, and the NNE–SSW Tcholliré-Banyo Shear Zone (Shandini et al. 2018; Nolla et al. 2015; Njamnsi et al. 2022b).

The geological history of the Koum basin can be divided into three main phases: the Pre-rift Phase, the Early Cretaceous Rifting Phase, and the Late Cretaceous Uplift and Inversion Phase. During the Early Cretaceous Rifting Phase, significant tectonic activity and sedimentation led to the formation of the basin. The Late Cretaceous Uplift and Inversion Phase resulted in the erosion of a substantial portion of the sedimentary fill. Post-rift processes, such as the uplift of the Cameroon Volcanic Line, further eroded approximately 2500 m of Upper Cretaceous and Paleogene sediments. The absence of Tertiary rifting and marine signatures suggests that the Koum basin represents a transitional zone between the West African Rift System (WARS) and the Central African Rift System (CARS) (Genik 1992, 1993; Guiraud and Maurin 1992; Fairhead 2020).

The Koum basin exhibits a typical rift basin depositional sequence, characterized by a basal fluvial unit overlain by a lacustrine unit and topped by a fluvial unit (Lambiase 1990). The Cretaceous deposits of the Koum basin, collectively known as the Koum Formation, are further subdivided into the lower Mbissirri Member and upper Gaba Sandstone Member (Fig. 2; Bessong et al. 2018; Njamnsi et al. 2022a, b; Agbor-Taku et al. 2023a, b; and Ngo Mandeng et al. 2024a, b).

The Mbissirri Member primarily consists of thick shale sequences interbedded with fine-grained mudstones, clay shales, thin limestones, and sandstones (Congleton 1990; Njamnsi et al. 2022b; Agbor-Taku et al. 2023a; Ngo Mandeng et al. 2024a). The member exhibits cyclical sedimentary patterns, with cross-bedded sandstones overlain by thicker mudstones. Paleontological evidence, including trace fossils, plant remains, and vertebrate fossils, suggests a lacustrine and fluvial depositional environment (Congleton et al. 1992; Nolla et al. 2015; Njamnsi et al. 2022b; Ngo Mandeng et al. 2024a).

The Gaba Sandstone Member is composed of medium- to coarse-grained sandstones, conglomerates, and interbedded mudstones and paleosols. This member represents a coarse-grained, braided fluvial system. Underlying the sedimentary fill is a Precambrian basement composed of various igneous and metamorphic rocks (Fig. 2). The Koum basin is renowned for its diverse assemblage of dinosaur footprints, particularly those of theropods and sauropods. Based on the fossil evidence, the basin has been tentatively assigned an Aptian age, correlating it with the early Cretaceous Elrhaz Formation in Niger (Dejax et al. 1989; Congleton 1990; Congleton et al. 1992).

3 Sampling and analytical methods

A total of 15 fresh, representative dark-gray, fine-grained mudstone samples were collected from the Koum basin (Fig. 3). Samples were obtained from outcrops in the Gouga, Kali, and Mayo Gaba localities, focusing on mudstones due to their potential organic matter content (Fig. 3; Table 1). The samples were subjected to mineralogical, whole-rock geochemical, and isotopic analysis.

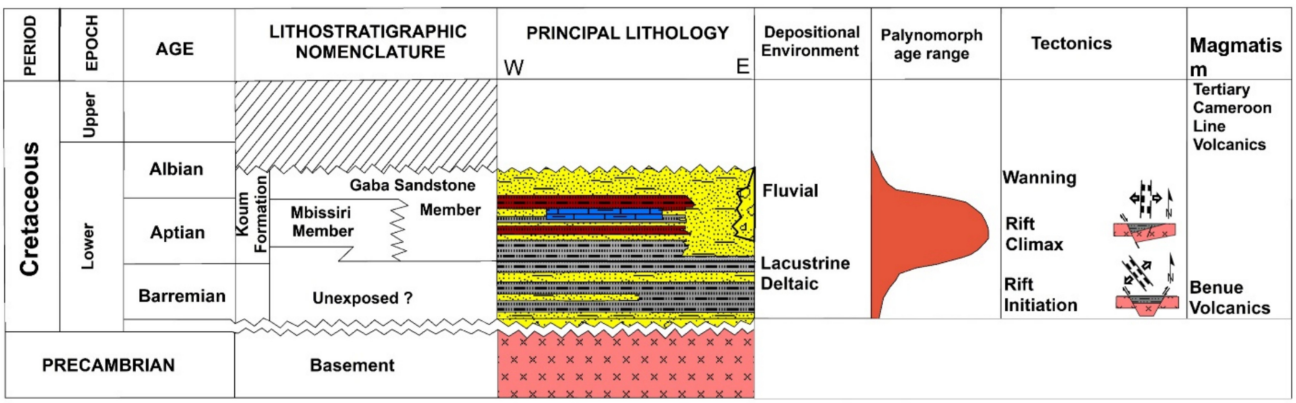

Fig. 2 Conceptual tectono-stratigraphy and gross depositional environments of the sedimentary fill of the Koum Basin (modified after Congleton 1990; Jacobs et al. 1996; Njamnsi et al. 2022b)

Fig. 3 Field photographs of mudstone outcrops in **a**, **c** Mayo Gaba locality (KAL009, KAL010, KAL011, KAL012, and KAL013), **d**, **f** Kali locality (KAL001, KAL002, KAL003, KAL004, KAL006, KAL007, and KAL008), and **g**, **I** Gouga locality (GOU001, GOU002 and GOU003)

Table 1 Summary of the analyzed mudstone samples

Lithotype	Sample ID	Analyses					
		XRD	XRF	ICP-MS	$\delta^{13}C_{VPDB}$	$\delta^{2}H_{VSMOW}$	$\delta^{18}O_{VSMOW}$
Gouga samples							
Dark gray marl	GOU001	X	X	X	X	X	X
Dark purple mudstone	GOU002	X	X	X	X	X	X
Gray shale	GOU003	X			X	X	X
Kali Samples							
Reddish-brown siltstone	KAL001	X	X	X	X	X	X
Brown claystone	KAL002	X	X	X	X	X	X
Reddish-brown mudstone	KAL003	X	X	X	X	X	X
Reddish-brown mudstone	KAL004	X	X	X	X	X	X
Gray shale	KAL006	X	X	X	X	X	X
Dark gray shales	KAL007	X			X	X	X
Gray claystone	KAL008	X			X	X	X
Mayo Gaba samples							
Dark gray mudstone	KAL009	X			X	X	X
Reddish-brown-purple mudstones	KAL010	X	X	X	X	X	X
Dark gray-black mudstones (shale)	KAL011	X	X	X	X	X	X
Dark gray-black mudstones (shale)	KAL012	X	X	X	X	X	X
Dark gray-black mudstones (shale)	KAL013	X			X	X	X

3.1 X-ray diffraction analyses

Mineralogical analyses were conducted at Queen's University, Ontario, Canada, using X-ray diffraction (XRD). Powdered samples were analyzed over an angular range of 5° to 80°, 2Θ for 60 s/step using Cu radiation (λ = 1.54 Å) and a PIXcel3D detector. Mineral identification was performed using the Highscore Pro 4.9 software and the International Center for Diffraction Data PDF-2 2020 database.

3.2 Bulk-rock geochemical analyses

Ten representative mudstone samples from the Koum basin were analyzed for major and trace element compositions at the Acme Analytical facility in Vancouver, Canada. For major element analyses, including SiO_2, Al_2O_3, K_2O, TFe_2O_3, Na_2O, CaO, MgO, P_2O_5, TiO_2, and MnO, each rock sample (up to 250 g) was pulverized to over 90% using an agate mill and analyzed by X-ray fluorescence (XRF) spectrometry after lithium borate ($Li_2B_4O_7/LiBO_2$) fusion and dilute nitric acid (HNO_3) digestion. Trace element concentrations were determined by inductively coupled plasma–mass spectrometry (ICP-MS) analysis, following aqua regia digestion. Loss on ignition was calculated by weight loss after ignition at 1000 °C. To ensure data quality, the equipment was washed with silica between samples. Analytical precision was within 5% for most elements, with detection limits ranging from 0.002 to 0.01 wt% for major elements and from 0.001 to 10 ppm for trace elements.

3.3 Stable isotope analyses

Stable carbon, hydrogen, and oxygen isotope analyses were conducted on 15 mudstone samples at Queen's University, Ontario, Canada.

Prior to carbon isotope analyses, the samples were treated with 20% hydrochloric acid (HCl) to remove carbonate minerals. The acid-treated samples were rinsed three times with high-purity (RO) water (15 MΩ resistivity) to remove residual acid. The rinsed samples were then dried overnight at 100 °C to remove any remaining moisture. The dried samples were weighed into tin capsules and the carbon isotopic composition of the samples was measured using a Thermo-Finnigan DeltaPlusXP Continuous-Flow Isotope Ratio Mass Spectrometer coupled to a Costech ECS 4010 Elemental Analyzer. The $\delta^{13}C$ values were reported in per mil (‰) relative to the Vienna Pee Dee Belemnite (VPDB) standard, with a precision of 0.2 ‰. The atmospheric $\delta^{13}C$ values were calculated using the following equation from Arens et al. (2000): $\delta^{13}Catm = (\delta^{13}Cplants + 18.67)/1.10$. This equation relates the $\delta^{13}C$ values of plant material to the atmospheric $\delta^{13}C$ values, allowing for the estimation of past atmospheric carbon isotope compositions.

The samples for oxygen isotope analyses were treated with 20% HCl to remove carbonate minerals. The acid-treated samples were rinsed three times with RO water (15 MΩ resistivity) to remove residual acid. The rinsed samples were dried overnight at 100 °C to remove any remaining moisture. The dried samples were weighed into silver capsules and the oxygen isotopic composition of the samples was measured using a MAT 253 Stable Isotope Ratio Mass Spectrometer coupled to a ThermoScientific TC/EA High Temperature Conversion Elemental Analyzer. The $^{18}O/^{16}O$ ratios in the sample were normalized to the Vienna Standard Mean Ocean Water (VSMOW) international standard. The $\delta^{18}O$ values were calculated based on the normalized ratios and were reported in per mil (‰) relative to the VSMOW standard, with a reproducibility of 0.3 ‰.

The samples for hydrogen isotope analyses were weighed into silver capsules and degassed for 1 h at 100 °C to remove any adsorbed water vapor. The degassed samples were crushed and loaded into a zero-blank autosampler purged with ultra-high purity helium (UHP He). The hydrogen isotopic composition of the samples was measured using a MAT 253 Stable Isotope Ratio Mass Spectrometer coupled to a Thermo Scientific TC/EA High Temperature Conversion Elemental Analyzer. The $\delta^{2}H$ values were calculated based on the measured hydrogen isotope ratios and were reported in per mil (‰) relative to the VSMOW standard, with a precision of 2 ‰.

4 Results

4.1 Bulk-rock mineralogical composition

The mudstones from the Koum basin exhibit a diverse mineralogical profile, primarily composed of phyllosilicates (~ 8.6%), feldspars (~ 30.5%), carbonates (~ 13.7%), and minor iron oxides (~ 2.7%) (Table 2; Fig. 4). Calcite (6.3%–41.6%), quartz (1.7%–70.7%), and albite (6.7%–74.3%) dominate the mineral assemblage, with significant variations in their proportions (Table 2). Additional minerals, including microcline, muscovite, vermiculite, hematite, illite, biotite, kaolinite, analcine, dolomite, ankerite, and anorthite, occur in varying amounts, reflecting diverse depositional and diagenetic processes (Table 2; Fig. 4). Microcline is present in selected samples (e.g., GOU001, KAL001), reaching up to 15.5%. Muscovite ranges from trace amounts to 12.1% in KAL009, while vermiculite appears sporadically, up to 3.2% (Table 2). Hematite is present in trace amounts, reaching 5.4% in KAL003. Illite is significant in some samples, up to 18.1% in KAL004, while biotite is minor, reaching 10.6% in KAL005 (Table 2). Kaolinite ranges from 0.3% to 19.9%, with KAL001 showing the highest content (19.9%). Analcine is present up to

Table 2 Bulk-rock mineralogy (%) for mudstone samples from the Koum basin

Sample ID	Calcite	Quartz	Albite	Microcline	Muscovite	Vermiculite	Hematite	Illite	Biotite	Kaolinite	Analcine	Dolomite	Ankerite	Anorthite
GOU001	18.00	17.70	42.10	15.50	4.10	2.60	0.00	0.00	0.00	0.00	0.00	0.00	0.00	0.00
GOU002	0.00	46.10	0.00	0.00	11.00	3.20	20.40	0.00	19.20	0.00	0.00	0.00	0.00	0.00
GOU003	41.60	25.80	29.20	0.00	1.00	2.40	0.00	0.00	0.00	0.00	0.00	0.00	0.00	0.00
KAL001	0.00	36.60	26.70	12.20	2.90	0.30	1.40	0.00	0.00	19.90	0.00	0.00	0.00	0.00
KAL002	0.00	23.30	34.10	0.00	2.70	0.80	3.60	0.00	0.00	12.90	0.00	0.00	0.00	0.00
KAL003	0.00	70.70	6.70	0.00	0.00	1.50	5.40	15.70	0.00	0.00	0.00	0.00	0.00	0.00
KAL004	17.40	11.60	27.70	0.00	0.00	2.00	0.00	18.10	0.00	0.00	23.30	0.00	0.00	0.00
KAL006	6.30	0.60	74.30	14.10	2.60	2.00	0.00	0.00	0.00	0.00	0.00	0.00	0.00	0.00
KAL007	20.20	28.30	44.60	5.70	0.00	1.10	0.00	0.00	0.00	0.00	0.00	0.00	0.00	0.00
KAL008	12.20	22.50	51.40	12.40	1.00	0.50	0.00	0.00	0.00	0.00	0.00	0.00	0.00	0.00
KAL009	13.40	1.70	33.00	0.00	12.10	2.90	0.00	0.00	0.00	0.00	36.90	0.00	0.00	0.00
KAL010	18.00	5.40	0.00	0.00	11.10	3.20	0.00	0.00	0.00	0.00	41.50	0.00	0.00	20.80
KAL011	15.00	22.20	31.00	0.00	0.00	1.40	0.00	0.00	2.30	0.00	8.30	19.80	0.00	0.00
KAL012	8.40	26.10	46.30	0.00	0.00	1.30	0.00	0.00	0.00	0.00	1.90	16.10	0.00	0.00
KAL013	6.30	30.10	38.70	9.70	0.00	1.60	0.00	0.00	3.00	0.00	0.00	0.00	10.50	0.00
Max	41.60	70.70	74.30	15.50	12.10	3.20	20.40	18.10	19.20	19.90	41.50	19.80	10.50	20.80
Min	0.00	0.60	0.00	0.00	0.00	0.30	0.00	0.00	0.00	0.00	0.00	0.00	0.00	0.00
Average	11.05	24.54	34.13	4.35	3.03	1.79	2.14	2.11	2.19	2.05	6.99	2.24	0.66	1.30

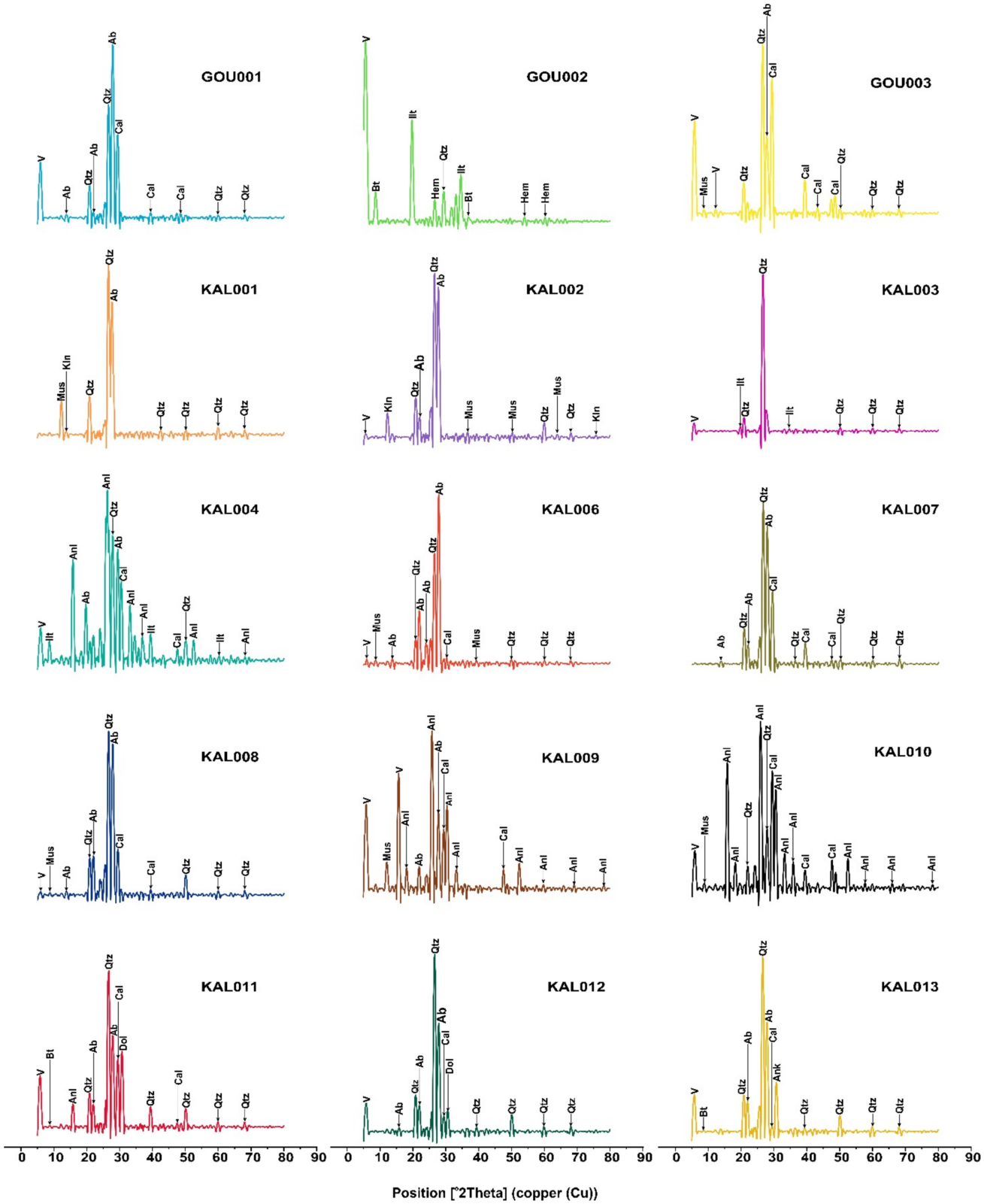

Fig. 4 X-ray diffraction patterns for mudstone samples (GOU001 to KAL013) from the Koum basin. *Ab* albite, *An* anorthite, *Ank* ankerite, *Anl* analcine, *Bt* biotite, *Ca* calcite, *Hem* hematite, *Il* illite, *Ka* kaolinite, *Mus* muscovite, *Qtz* quartz, *V* vermiculite

36.9% in KAL009. Dolomite is present in trace amounts, while ankerite reaches 20.8% in KAL010. Anorthite is found only in KAL013 at ~ 10.5% (Table 2).

4.2 Bulk-rock geochemical composition

The bulk-rock major and trace element concentration for the studied mudstone samples from the Koum basin are listed in Table 3 and ESM_1 (Online Resource).

4.2.1 Major elements

The mudstones are primarily composed of SiO_2 (37.18–66.31 wt%), with lower amounts of Fe_2O_3 (3.15–11.58 wt%). Other major oxides, such as Al_2O_3 (9.08–17.01 wt%), CaO (0.37–22.95 wt%), K_2O (0.98–4.11 wt%), and Na_2O (0.42–5.47 wt%), exhibit variable concentrations (Table 3). Minor elements, including MnO (0.02–0.41 wt%), TiO_2 (0.40–1.14 wt%), and P_2O_5 (0.10–0.39 wt%) are present in low amounts (Table 3). Compared to the average Post-Archaean Australian Shale (PAAS; Taylor and McLennan 1985), the Koum mudstones are enriched in Na_2O, CaO, MgO, and P_2O_5 but depleted in other major elements (Table 3). The geochemical ratios of Al_2O_3/TiO_2 (17.56), K_2O/Al_2O_3 (0.19), K_2O/Na_2O (1.77) and SiO_2/Al_2O_3 (4.0) suggest the presence of clay minerals, K-bearing minerals and quartz (Table 3). Positive correlations between K_2O and Al_2O_3 ($R^2 = 0.81$; Fig. 5a) and SiO_2 and Al_2O_3 ($R^2 = 0.52$; Fig. 5b) confirms the association of K and Al within feldspars and clay minerals (e.g., kaolinite, illite, vermiculite). Based on the $\log(Fe_2O_3/K_2O)$ vs. $\log(SiO_2/Al_2O_3)$ classification diagram, after Herron (1988), the samples are categorized as shales (Fig. 6).

4.2.2 Trace elements

The Koum mudstones exhibit low concentrations of most analyzed trace elements, with notable exceptions including Sr (64.9–747.3 ppm), Ba (56–485.1 ppm), V (46–111 ppm), Ni (16.4–48.9 ppm), Cr (40.9–86.9 ppm), Ag (7–71 ppm), Cu (10.5–80.2 ppm), Rb (18.8–82.3 ppm), Zn (52.9–133.4 ppm), La (19.1–76.8 ppm), and Ce (33.1–121.9 ppm) as shown in ESM_1. When normalized to the Upper Continental Crust (UCC; Rudnick and Gao 2014), the mudstones show depletions in Ba, Nb, Hf, and Zr (Fig. 7), while elements including Ni, Cr, Co, Th, La, Ce, Pb, and Ti have roughly similar concentrations to UCC (Fig. 7). Enrichment factor analysis, expressed as $EF_{average} = (element/Ti)_{sample} / (element/Ti)_{PAAS}$ (Tribovillard et al. 2006), revealed that Zn, Sr, and Mo have elevated concentrations (EF values > 1) compared to the PAAS average, while Co, V, Cu, and Ni show lower concentrations (Fig. 8).

Table 3 Major element compositions (wt%) for mudstone samples from the Koum basin

Sample	KAL001	KAL002	KAL003	KAL004	KAL006	KAL010	KAL011	KAL012	GOU001	GOU002	Average	PAAS
SiO_2	64.68	65.87	66.31	66.11	52.64	64.01	47.36	37.18	38.35	50.14	55.27	62.80
Al_2O_3	15.81	15.95	15.61	14.53	15.50	17.01	10.11	9.08	9.39	16.90	13.99	18.90
K_2O	4.11	4.10	3.90	2.37	1.60	4.00	1.16	0.98	1.69	3.77	2.77	3.70
TFe_2O_3	7.52	6.25	6.89	5.84	10.24	6.50	4.65	4.56	3.15	11.58	6.72	7.22
Na_2O	2.83	3.04	2.84	1.98	5.47	2.41	3.67	3.46	2.03	0.42	2.82	1.20
CaO	0.63	0.62	0.37	1.14	2.14	0.66	9.67	10.04	22.95	2.23	5.05	1.30
MgO	0.83	0.77	0.70	2.96	4.16	0.90	3.37	3.22	2.27	6.07	2.53	2.20
MnO	0.04	0.06	0.03	0.05	0.09	0.02	0.09	0.12	0.41	0.09	0.10	0.11
P_2O_5	0.29	0.25	0.14	0.23	0.16	0.39	0.10	0.15	0.21	0.25	0.22	0.16
TiO_2	1.07	0.89	1.14	1.05	0.78	1.05	0.46	0.40	0.82	0.73	0.84	1.00
LOI	2.20	2.50	2.30	4.30	7.70	3.30	19.10	30.60	19.40	7.60	9.90	6.00
Total	100.01	100.30	100.23	100.56	100.48	100.25	99.74	99.79	100.67	99.78	100.18	104.59
Al_2O_3/TiO_2	14.78	17.92	13.69	13.84	19.87	16.20	21.98	22.70	11.45	23.15	17.56	18.90
K_2O/Al_2O_3	0.26	0.26	0.25	0.16	0.10	0.24	0.11	0.11	0.18	0.22	0.19	0.20
K_2O/Na_2O	1.45	1.35	1.37	1.20	0.29	1.66	0.32	0.28	0.83	8.98	1.77	3.08
SiO_2/Al_2O_3	4.09	4.13	4.25	4.55	3.40	3.76	4.68	4.09	4.08	2.97	4.00	3.32
P_2O_5/TiO_2	0.27	0.28	0.12	0.22	0.21	0.37	0.22	0.38	0.26	0.34	0.27	0.16

LOI loss on ignition, *PAAS* Post Archean Australia Shale (Taylor and McLennan 1985)

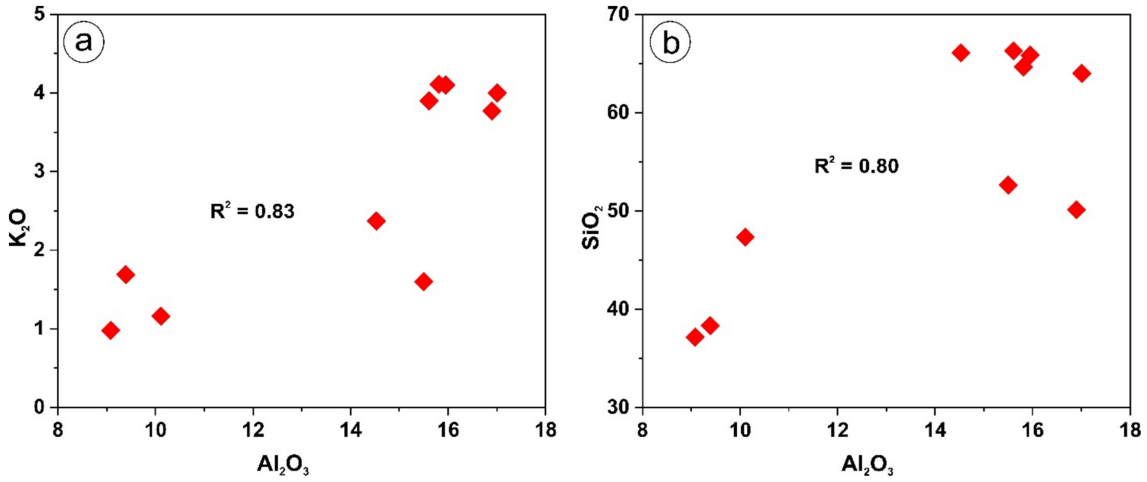

Fig. 5 Binary plots showing the relation between selected major oxides in the Koum mudstones: **a** Al_2O_3 versus K_2O and **b** Al_2O_3 versus SiO_2

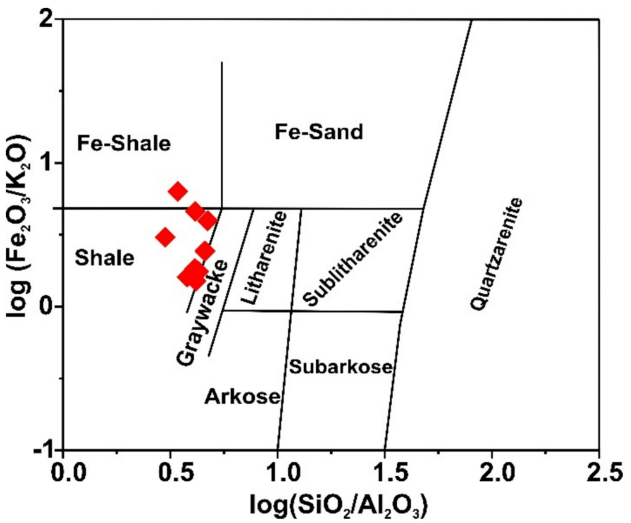

Fig. 6 Geochemical classification of the Koum mudstones based on the log (SiO_2/Al_2O_3) versus log (TFe_2O_3/K_2O) diagram, as proposed by Herron (1988)

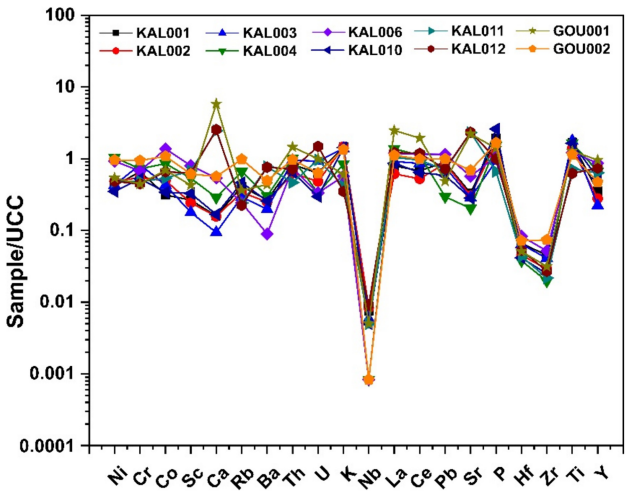

Fig. 7 Upper continental crust (UCC)-normalized multi-elemental variation diagrams for the Koum mudstones. UCC data from McLennan (1989)

4.3 Stable isotope composition

Table 4 presents the $\delta^{13}C$, $\delta^{18}O$, and $\delta^{2}H$ values for the studied mudstones, reported in parts per mil (‰) relative to VPDB and VSMOW, respectively.

4.3.1 $\delta^{13}C_{VPDB}$ composition

The Koum mudstones exhibit a range $\delta^{13}C$ values from − 25.2 ‰ to − 35.2 ‰, with an average of − 28.2 ‰ ($n = 15$; Table 4). Samples from the Gouga locality show a narrow range of $\delta^{13}C$ values (− 25.8 ‰ to − 27.6 ‰), which are slightly more positive than the overall average (Table 4). The Kali samples, on the other hand, exhibit a wider range of $\delta^{13}C$ values (− 25.2 ‰ to − 35.2 ‰), with a particularly low value for sample KAL002 (− 35.2 ‰), which is significantly more negative than the overall average (Table 4). The Mayo Gaba samples generally have more negative $\delta^{13}C$ values (− 27.7 ‰ to − 31.0 ‰), with a trend toward lower $\delta^{13}C$ values in samples KB-KAL011 (− 30.0 ‰), KAL012 (− 29.7 ‰), and KAL013 (− 31.0 ‰), except for KAL010, with a slightly more positive $\delta^{13}C$ value of − 27.7 ‰ (Table 4).

4.3.2 $\delta^{18}O_{VSMOW}$ composition

The $\delta^{18}O$ values of the Koum mudstones range from + 3.6‰ to + 24.9‰ with an average of + 12.2‰ ($n = 15$; Table 4). Samples from the Gouga locality have $\delta^{18}O$ values

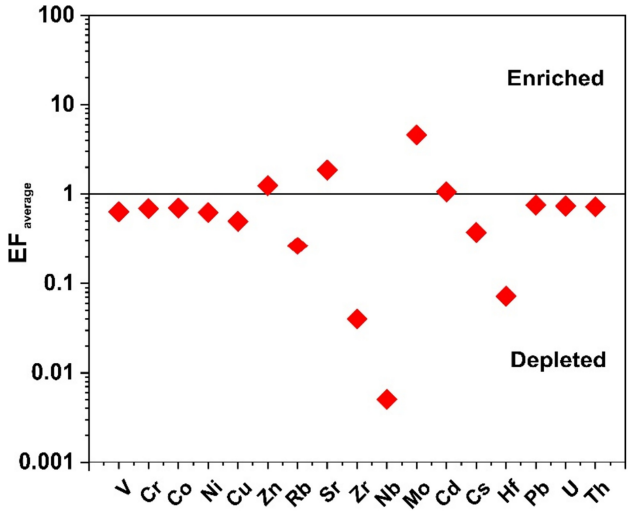

Fig. 8 PAAS-normalized trace element plot for the Koum mudstones. PAAS data from Taylor and McLennan (1985). $EF_{average}$, a geochemical normalization index, was calculated as $(element/Ti)_{sample}/(element/Ti)_{PAAS}$ (Tribovillard et al. 2006)

Table 4 Carbon, hydrogen and oxygen isotope compositions for mudstone samples from the Koum basin

Sample ID	δ^{13}Corg (‰VPDB)	δ^{2}H (‰VSMOW)	$\delta^{18}O_{TCEA}$ (‰VSMOW)	δ^{13}Catm
GOU001	− 26.9	− 56	16.1	− 7.6
GOU002	− 27.6	− 81	5.7	− 8.2
GOU003	− 25.8	− 58	21.7	− 6.6
KAL001	− 28.4	− 58	4.0	− 8.9
KAL002	− 35.2	− 62	3.6	− 15.1
KAL003	− 25.9	− 78	4.9	− 6.6
KAL004	− 25.2	− 66	9.2	− 6.0
KAL006	− 26.1	− 51	9.3	− 6.8
KAL007	− 27.1	− 52	19.8	− 7.8
KAL008	− 26.5	− 52	14.7	− 7.2
KAL009	− 30.3	− 50	7.6	− 10.6
KAL010	− 27.7	− 52	11.6	− 8.2
KAL011	− 30.0	− 104	24.9	− 10.4
KAL012	− 29.7	− 100	18.7	− 10.1
KAL013	− 31.0	− 99	22.3	− 11.3
Max	− 25.2	− 50.0	24.9	− 6.0
Min	− 35.2	− 103.5	3.6	− 15.1
Average	− 28.2	− 68.0	12.9	− 8.8

$\delta^{13}Catm = (\delta^{13}C_{plants} + 18.67) / 1.10$ (Arens et al. 2000)

between + 5.7‰ and + 21.7‰, with an average of + 14.5‰ (Table 4). The δ^{18}O values for the Kali samples range from + 3.6 ‰ to + 19.8‰, with an average of + 10.5‰. The Mayo Gaba samples generally exhibit higher δ^{18}O values (+ 7.6‰ to + 24.9‰; Table 4), with samples KAL011 and KAL013 showing the highest δ^{18}O values of + 24.9‰ and + 22.3‰ respectively (Table 4).

4.3.3 $\delta^{2}H_{VSMOW}$ composition

The δ^{2}H values of the Koum mudstones range from − 104‰ to − 50‰ with an average of − 68‰ ($n = 15$). The Gouga (− 56‰ to − 81‰) and Kali (− 51‰ to − 78‰) samples exhibits less negative δ^{2}H values compared to the Mayo Gaba samples, which show more negative δ^{2}H values (− 50‰ to − 104‰), particularly samples KAL011(− 104 ‰), KAL012 (− 100 ‰), and KAL013 (− 99 ‰).

5 Discussions

5.1 Paleoweathering

Several geochemical indices, including the Chemical Index of Alteration (CIA), the Index of Compositional Variability (ICV), and the Plagioclase Index of Alteration (PIA), are commonly used to assess the degree of weathering in sedimentary rocks (Nesbitt and Young 1982; Fedo et al. 1995; Cox et al. 1995; Price and Velbel 2003; Roddaz et al. 2006; Bauluz et al. 2000). The CIA values for unweathered igneous rocks such as basalts (30–45) and granitoids (45–55), are lower compared to moderately weathered Phanerozoic shales (70–75), which contain minerals like muscovite, illite, and kaolinite (Cox et al. 1995). A high ICV value indicates a high degree of compositional variability, suggesting a less mature sedimentary rock with a significant amount of silicate minerals other than clay. These rocks often form in tectonically active settings. Conversely, a low ICV value indicates a compositionally mature sedimentary rock, enriched in clay minerals and typically derived from mature sediments or Cratonic environments (Cox et al. 1995; Van de Kamp and Leake 1985).

Comparison of the Koum mudstones to PAAS values (Taylor and McLennan 1985) reveals minor depletions in some major elements including SiO_2, Al_2O_3, K_2O, and Fe_2O_3 and slight enrichments in others such as Na_2O, CaO, and P_2O_5, suggesting a low to moderate degree of weathering (Table 3). The CIA (41.06−65.70) and PIA (40.11−72.98) values (Table 5) support this finding, indicating a source area with a mix of minimally to moderately weathered rocks. The low ICV values (average 1.64; Table 5) and mineral composition of the Koum mudstones, including the abundance of albite (~ 39%) and low amounts of clay minerals such as vermiculite (~ 2%), biotite (~ 9%), kaolinite (~ 16%), illite (~ 17%), and muscovite (~ 6%), suggests a relatively immature source area (Tables 2, Fig. 4). This implies rapid erosion and deposition of first-cycle material in a tectonically active setting,

Table 5 Paleoweathering and paleoenvironment parameters for the Koum mudstones

Sample	*N*-value	*C*-value	PIA	CIA	ICV	A/NK	A/CNK	TOC(%)	C_{org}/P
KAL001	5.25	0.90	66.21	60.68	1.07	1.74	1.54	0.04	0.36
KAL002	4.83	0.74	65.26	60.15	0.98	1.69	1.51	0.04	0.41
KAL003	4.48	0.89	68.07	62.01	1.01	1.76	1.63	0.02	0.37
KAL004	20.37	0.70	69.20	64.80	1.06	2.50	1.84	0.03	0.34
KAL006	26.84	0.77	51.63	51.44	1.57	1.44	1.06	0.03	0.48
KAL010	5.29	0.82	71.03	64.15	0.91	2.05	1.79	0.11	0.73
KAL011	33.33	0.26	41.08	42.01	2.27	1.39	0.72	6.91	178.34
KAL012	35.46	0.26	40.11	41.06	2.50	1.34	0.70	5.48	94.29
GOU001	24.17	0.12	51.82	51.45	3.50	1.82	1.06	0.02	0.25
GOU002	35.92	0.93	72.98	65.70	1.47	3.54	1.91	0.02	0.21

N-value = 100 × MgO/Al_2O_3 (after Chen et al. 2022); C-value = Σ(Fe + Mn + Cr + Ni + V + Co)/Σ(Ca + Mg + Sr + Ba + K + Na) (after Fedo et al. 1995); A/CNK = molar $Al_2O_3/(CaO + Na_2O + K_2O)$ and A/NK = molar $Al_2O_3/(Na_2O + K_2O)$ (after Nesbitt and Young 1989); ICV = [$(Fe_2O_3 + K_2O + Na_2O + CaO + MgO + TiO_2)/Al_2O_3$] (after Cox et al. 1995); CIA = [molar $Al_2O_3/(Al_2O_3 + CaO + Na_2O + K_2O) \times 100$] (after Nesbitt and Young 1982); PIA = [molar $(Al_2O_3–K_2O)/(Al_2O_3–K_2O + Na_2O + CaO) \times 100$] (after Fedo et al. 1995); C_{org}/P = (TOC/12)/(P/30.97) (after Algeo and Ingall 2007). TOC values are from Njamnsi et al. (2022b)

consistent with previous studies on the Koum basin and Upper Benue Trough (Ngo Mandeng et al. 2024a; Tchouatcha et al. 2021).

On the A-(Al_2O_3)-CN (CaO + Na_2O)-K (K_2O) triangular plot of molecular proportions after Nesbitt and Young (1989), the Koum mudstones align with the adamellite–granodiorite/granite weathering trend (Fig. 9a). This alignment is consistent with the provenance of the mudstones as discussed in Sect. 5.2. The Th/U ratio is a useful tool for assessing the extent of weathering in source areas. Under surficial oxidizing conditions, U is more mobile than Th, which tends to concentrate in residual materials (McLennan 2001; López et al. 2005). High Th/U ratios (> 4.0) indicate intense weathering or sedimentary recycling (McLennan et al. 1993; Partin et al. 2013). The elevated Th/U ratio of the Koum mudstones (~ 5.85; ESM_1), compared to the PAAS (4.71) and UCC (3.89) values, indicates a moderate degree of weathering and recycling in the source area.

While the CIA value and the A–CN–K diagram (Nesbitt and Young 1989) are commonly used to assess chemical weathering in sedimentary rocks, the CIA value primarily reflects the weathering of feldspars in felsic rocks and does not account for the behavior of divalent metals (e.g., Fe^{2+}, Mg^{2+}, Mn^{2+}) found in mafic minerals. The A–CN–K system also overlooks SiO_2, a major component of silicate minerals. Moreover, studies by Meunier et al. (2013) and Li and Yang (2010) showed that the CIA value can be influenced by source rock composition, post-depositional processes (e.g., diagenesis, metamorphism), and drainage basin heterogeneity, rather than solely reflecting chemical weathering. Consequently, the CIA value may record long-term regional weathering trends that do not directly correspond to environmental conditions at the time of sediment deposition.

Given these limitations, we interpret the CIA and A–CN–K results alongside other geochemical indicators, such as the M^+–4Si–R^{2+} system (where $M^+ = Na^+ + K^+ + 2Ca^{2+}$; 4Si = Si/4; $R^{2+} = Fe^{2+} + Mg^{2+}$) which integrates variations in alkali, alkaline earth, silica, and divalent cations (Meunier et al. 2013). When plotted in M^+–4Si–R^{2+} space, the Koum mudstones cluster between the felsic and mafic compositional fields (Fig. 9b, c). The co-variation of Δ4Si% with the $R^{3+}/(R^{3+} + R^{2+} + M^+)$ ratio provides a more robust insight into the nature of the source rocks and the degree of weathering (Meunier et al. 2013). High $R^{3+}/(R^{3+} + R^{2+} + M^+)$ values (approaching 1) and Δ4Si% values greater > 50% indicate intense chemical weathering and residual enrichment of immobile elements, while lower values suggest limited alteration.

The $R^{3+}/(R^{3+} + R^{2+} + M^+)$ ratio, reflecting the enrichment of immobile trivalent cations (e.g., Al^{3+}, Fe^{3+}) relative to mobile monovalent and divalent cations, serves as a sensitive weathering indicator (Meunier et al. 2013). In the Koum mudstone samples, the $R^{3+}/(R^{3+} + R^{2+} + M^+)$ values range from 0.19 to 0.67, with most falling between 0.53 and 0.67 (Table 6), suggesting moderate chemical weathering through the leaching of mobile elements and enrichment of trivalent cations. Lower ratios (0.19–0.31) exhibited by some of the samples indicate less intense weathering or input from more mafic, chemically immature sources (Table 6). On the $R^{3+}/(R^{3+} + R^{2+} + M^+)$ versus Δ4Si% plot (after Meunier et al. 2013), most of the Koum mudstone samples fall between the granitic and mafic trends, reflecting a source region composed of minimally to moderately weathered rocks (Fig. 9d).

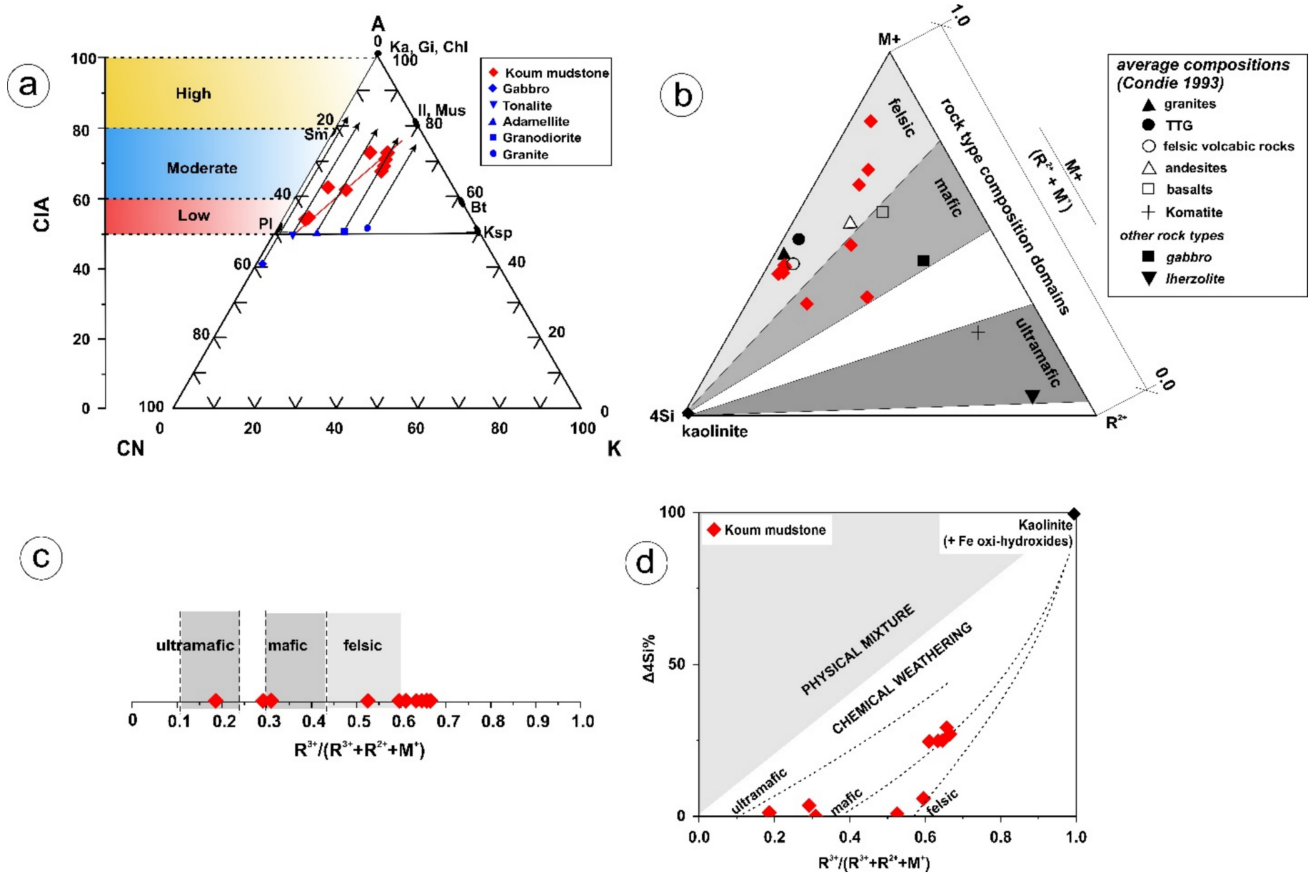

Fig. 9 The composition of the Koum mudstones is plotted in **a** the A-CN-K ternary plot of Nesbitt and Young (1984); **b** the M^+–4Si–R^{2+} system (Meunier et al. 2013); **c** the representative domains of the major rock groups, scaled in the $R^{3+}/(R^{3+} + R^{2+} + M^+)$ coordinate; and **d** the Δ4Si% vs. $R^{3+}/(R^{3+} + R^{2+} + M^+)$ diagram (Meunier et al. 2013). The *dark arrows* in **a** indicate weathering trends of igneous rocks (gabbro, tonalite, adamellite, granodiorite, and granite). *Bt* biotite, *Chl* chlorite, *Gi* gibbsite, *Il* illite, *Ka* kaolinite, *Ksp* K-feldspar, *Mus* muscovite, *Pl* plagioclase, *Sm* smectite. For the calculation of the M^+, 4Si, R^{2+}, R^{3+}, $R^{3+}/(R^{3+} + R^{2+} + M^+)$, and Δ4Si% parameters, see Table 6 for details

Table 6 Composition parameters for the Koum mudstones in the M^+–4Si–R^{2+} system

Sample	Bulk composition					Normalized parameters				
	4Si	M^+	R^{2+}	R^{3+}	$R^{3+}/R^{3+} + R^{2+} + M^+$	$4Si + M^+ + R^{2+}$	4Si%	M^+%	R^{2+}%	Δ4Si%
KAL001	269.10	201.05	20.60	404.30	0.65	490.74	54.83	40.97	4.20	24.97
KAL002	274.05	207.26	19.11	391.14	0.63	500.41	54.76	41.42	3.82	24.86
KAL003	275.88	187.64	17.37	392.49	0.66	480.89	57.37	39.02	3.61	29.18
KAL004	275.05	154.87	73.45	358.16	0.61	503.36	54.64	30.77	14.59	24.65
KAL006	219.00	286.80	103.23	432.29	0.53	609.03	35.96	47.09	16.95	0.87
KAL010	266.31	186.23	22.33	415.07	0.67	474.87	56.08	39.22	4.70	27.04
KAL011	197.04	487.92	83.62	256.55	0.31	768.58	25.64	63.48	10.88	0.05
KAL012	154.68	490.52	79.90	235.22	0.29	725.10	21.33	67.65	11.02	3.59
GOU001	159.55	919.86	56.33	223.64	0.19	1135.74	14.05	80.99	4.96	1.20
GOU002	208.60	173.12	150.62	476.53	0.60	532.35	39.19	32.52	28.29	5.86

$4Si = Si/4$; $M^+ = Na^+ + K^+ + 2Ca^{2+}$; $R^{2+} = Mg^{2+} + Fe^{2+} + Mn^{2+}$; $R^{3+} = Al^{3+} + Fe^{3+}$; $\Delta4Si\% = [(4Si_{altered\ sample} — 4Si_{unaltered\ parent\ rock}) \times 100]/(100 — 4Si_{unaltered\ parent\ rock})$, after Meunier et al. (2013). The source rock is considered to be represented by the average upper continental crust (Condie 1993), where 4Si% = 39.8

5.2 Sediment source

Geochemical analysis of mudstones, is a valuable tool for determining the source of sediments. This is because mudstones are relatively homogeneous and less susceptible to post-depositional alteration (Cox et al. 1995; Cullers et al. 1988, 1994; Hayashi et al. 1997; Zhang et al. 2022; Tao et al. 2017; Wu et al. 2024). The K_2O/Al_2O_3 ratio is a commonly used proxy for provenance assessment (Cox et al. 1995). Low K_2O/Al_2O_3 ratios (< 0.3) indicate a clay-rich sources, while higher ratios (0.4–1.0) suggest a significant contribution from alkali feldspar. The low K_2O/Al_2O_3 ratio (~ 0.19) for the Koum mudstones indicates a clay-rich source (Table 3). Major element ratios, such as Al_2O_3/TiO_2, are often used to discriminate between different source rock types. Mafic sources generally yield Al_2O_3/TiO_2 ratios below 14, while intermediate igneous sources yield Al_2O_3/TiO_2 ratios that typically fall between 19 and 28 (Girty et al. 1996; Hayashi et al. 1997). The Al_2O_3/TiO_2 ratios (11.45–23.15) for the Koum mudstones (Table 3, Fig. 10a), suggests an intermediate igneous source. Additional geochemical indicators, such as the K_2O/Na_2O ratio (~ 1.77), TiO_2/Zr ratio (~ 0.14), Na_2O (~ 2.82 wt%), MgO (~ 2.53 wt%), P_2O_5 (~ 0.22 wt%), and SiO_2 (~ 55.27 wt%) contents (Table 3; Fig. 10b), further support this interpretation. These findings are consistent with recent study on the Koum basin (Ngo Mandeng et al. 2024a).

Trace element ratios, such as Zr/Sc, Th/Sc, La/Sc, Sc/Th, and La/Th, are useful tools for determining the source of sedimentary rocks. Elements like Sc, La, Th, and Hf are relatively resistance to weathering and diagenesis, making them reliable indicators of source rock composition (Condie 1993; Taylor and McLennan 1985; Wronkiewicz and Condie 1987; McLennan et al. 1993; Floyd and Leveridge 1987). The Sc/Th ratio, in particular, can be used to differentiate between felsic and mafic sources (McLennan 1991; Lyubetskaya and Korenaga 2007). Crustal sources typically have lower Sc/Th ratios (~ 1.33) and higher La/Sc ratios (~ 2.7) compared to

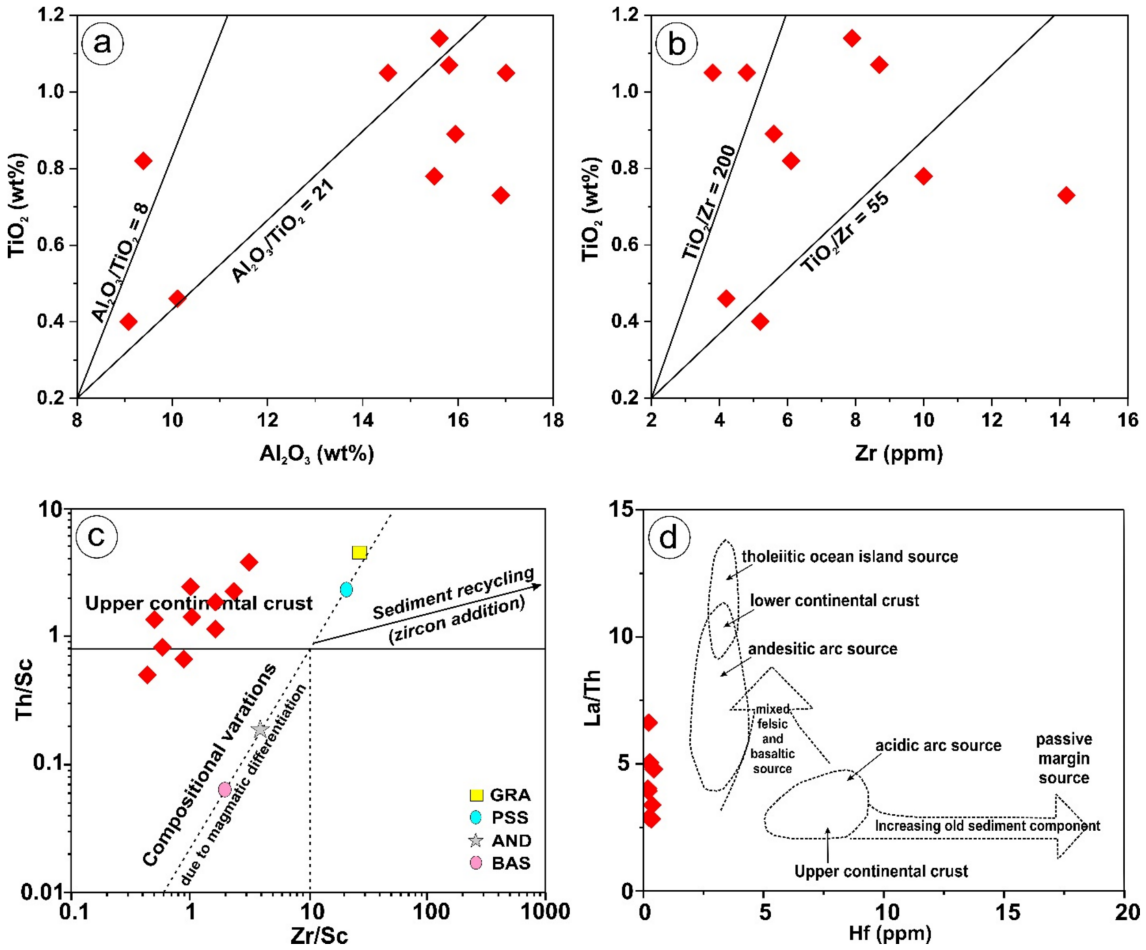

Fig. 10 Bivariate plots showing the provenance of Koum mudstones: **a** Al_2O_3 versus TiO_2 (Hayashi et al. 1997), **b** Zr versus TiO_2 (Hayashi et al. 1997), **c** Zr/Sc versus Th/Sc (McLennan et al. 1993), and **d** Hf versus La/Th (Floyd and Leveridge 1987). *AND* andesite, *BAS* basalt, *GRA* granite, *PSS* passive margin sandstone

mafic sources with Sc/Th ratios near 20.3 and lower La/Sc ratios near 0.91 (Taylor and McLennan 1981; McDonough and Sun 1995; Lyubetskaya and Korenaga 2007; Rudnick and Gao 2014). The Koum mudstones exhibits a La/Sc ratio (~ 6.30), significantly higher than that of mafic sources and a Sc/Th ratio (~ 0.84) slightly lower than the typical crustal value (ESM_1). These geochemical ratios, with the positioning of the samples on Th/Sc vs. Zr/Sc and La/Th vs. Hf diagrams, further supports an intermediate igneous provenance (Fig. 10c, d). The plotting of the samples between the felsic and mafic compositional domains of the M^{+}–4Si–R^{2+} coordinate system and on the $R^{3+}/(R^{3+} + R^{2+} + M^{+})$ vs. Δ4Si% diagram of Meunier et al. (2013) confirms contributions from felsic source rocks, such as granites, with some input from mafic lithologies (Fig. 9b–d).

5.3 Paleoclimate and paleoenvironmental conditions

5.3.1 Constraints from bulk-rock mineralogy

The mineralogical composition of mudstones is a valuable tool for reconstructing past environments and climates (e.g., Thiry 2000; Ruffell et al. 2002; Fagel et al. 2007; Lanson et al. 2009; Bristow et al. 2009; Dudek et al. 2012; Deconinck et al. 2020). The composition of mudstones often reflects the dominant weathering regime (physical and/or chemical), which is influenced by climate (Weaver 1989). Additionally, variations in the CIA index of mudstones, which is linked to plagioclase leaching, can provide insights into weathering intensity and past humidity levels (Nesbitt and Young 1982, 1989). The Koum mudstones, with their minimal diagenetic alteration, are well-suited for paleoenvironmental reconstruction (Table 2; Fig. 4).

The Koum mudstones are predominantly composed of calcite (6.3%–41.6%), quartz (1.7%–70.7%), and albite (6.7%–74.3%), with minor amounts of microcline, muscovite, vermiculite, hematite, illite, biotite, kaolinite, dolomite, ankerite and anorthite (Table 2; Fig. 4). The mineral assemblage reflects a complex interplay of depositional and diagenetic processes. The presence of minerals like zeolites (analcine) and carbonates (ankerite, dolomite), suggests potential low-grade metamorphism or hydrothermal alteration (Table 2). Kaolinite, indicative of weathering under warm and humid conditions and illite, associated with limited hydrolysis and dry environments, suggests variable climatic conditions during deposition (Chamley 1989; Thiry 2000; Velde 1995; Li et al. 2000; Adatte et al. 2002; Deconinck et al. 2003, 2019; Gertsch et al. 2011; Charbonnier et al. 2020).

The low kaolinite content in samples KAL001 (~ 19.90%) and KAL002 (~ 12.90%), coupled with the low detrital illite content in samples KAL003 (~ 15.70%) and KAL004 (~ 18.10%), indicates limited chemical weathering, suggesting a transition between humid and drier or semi-arid conditions (Table 2). The presence of vermiculite indicates alteration of biotite and muscovite to trioctahedral and dioctahedral vermiculite, respectively, likely due to high precipitation and chemical weathering (Walker 1975; Moore and Reynolds 1997). The overall clay mineral composition suggests similar climatic conditions and depositional environment in the Gouga, Kali and Mayo Gaba localities.

The dominance of quartz (1.7%–70.7%) in the Koum mudstones suggests a low degree of alteration and short transport distances (Table 2; Fig. 4). The low CIA values (~ 56.35; Table 5) coupled with the position of the mudstones on the SiO_2 vs. $Al_2O_3 + K_2O + Na_2O$ discrimination diagram after Suttner and Dutta (1986), further support a semi-arid climatic setting (Fig. 11). These findings are consistent with those of previous studies on the Koum basin and Upper Benue Trough, which also suggested semi-arid conditions (Bessong et al. 2018; Tchouatcha et al. 2021; Njamnsi et al. 2022a, b; Ngo Mandeng et al. 2024a, b).

However, major element-based indices reflect broader compositional trends that are influenced by multiple factors, including provenance, weathering intensity, and mineral stability, which may not directly align with trace element-based paleoclimate proxies. While a major element dataset (SiO_2 vs. $Al_2O_3 + K_2O + Na_2O$) generally supports deposition under semi-arid conditions, there is the need for a multiproxy approach that takes into consideration both major and trace element concentrations to appropriately interpret the paleoclimatic condition, especially in altered sedimentary settings like the Koum basin.

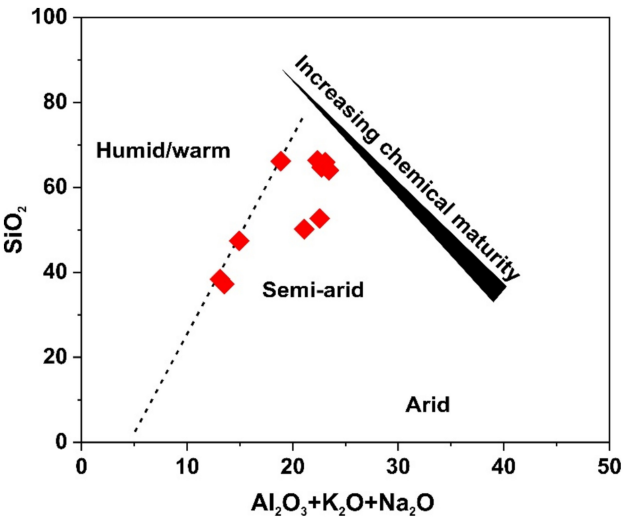

Fig. 11 SiO_2 versus $Al_2O_3 + K_2O + Na_2O$ plot (Suttner and Dutta 1986) showing the climatic conditions during the formation of the Koum mudstones

5.3.2 Constraints from bulk-rock geochemistry

Past environmental conditions including paleosalinity can be estimated using various geochemical proxies. Two commonly employed proxies are the Sr/Ba ratio and the *N*-value ($100 \times MgO/Al_2O_3$), which exhibit strong correlations with water salinity (Chen et al. 2022; Zhang et al. 2023). As water salinity increases, the Sr/Ba ratio also rises. This is because Ba^{2+} ions, being more reactive than Sr^{2+} ions, preferentially combine with sulfate (SO_4^{2-}) to form insoluble precipitates (Walker et al. 1963). The *N*-value proxy leverages the contrasting behavior of Mg and Al. Magnesium is primarily associated with marine environments, while Al is more indicative of terrestrial sources (Tian et al. 2014). Based on these proxies, paleosalinity can be categorized as freshwater (Sr/Ba < 0.2, *N*-value < 1), brackish water (0.2 < Sr/Ba < 0.5, 1 < *N*-value < 10), and saline water (Sr/Ba > 0.5, *N*-value > 10) (Meng et al. 2012; Wei & Algeo 2020; Chen et al. 2022; Wu et al. 2024). The Koum mudstones, with their Sr/Ba ratios of 0.34–3.25 (ESM_1) and *N*-values from 4.48 to 35.92 (Table 5), exhibit characteristics of both brackish and saline environments.

Paleoclimate and paleosalinity are interconnected since arid conditions can result to increased salinity (Chen et al. 2020). Paleoclimate can be reconstructed using proxies such as the *C*-value and the Sr/Cu ratio (Lerman et al. 1995; Zhao et al. 2007; Jia et al. 2013). The *C*-value, a geochemical index calculated as Σ(Fe + Mn + Cr + Ni + V + Co)/Σ(Ca + Mg + Sr + Ba + K + Na), suggests that elements including Fe, Mn, and Cr are primarily enriched in moist environments, while elements such as Ca, Mg, and Sr tend to be enriched in arid environments (Zhao et al. 2007; Cao et al. 2012). The Sr/Cu ratio is a useful proxy for paleoclimate reconstruction, with higher values typically indicating drier conditions and lower values suggesting wetter periods (Lerman 1995; Meng et al. 2012; Jia et al. 2013). However, interpretations vary with some studies defining Sr/Cu > 10 as arid and 1–10 as warm and humid (Wang et al. 1997; Hu et al. 2012; Qu et al. 2019), while other studies propose Sr/Cu > 5 for arid climates and 1.3–5 for humid conditions (Lerman 1987; Hu et al. 2017). This inconsistency underscores the need for the integration of multiple geochemical proxies for a more reliable paleoclimate interpretation. The *C*-value index provides a more quantitative assessment of paleoclimate, categorizing environments as arid (*C*-value < 0.2), semi-arid (0.2 ≤ *C*-value < 0.4), semi-arid to semi-moist (0.4 ≤ *C*-value < 0.6), semi-moist (0.6 ≤ *C*-value < 0.8) and moist (*C*-value ≥ 0.8) (Moradi et al. 2016; Wang et al. 2022; Wu et al. 2024).

The wide range of Sr/Cu ratios (1.88–37.47; ESM_1) and C-values (0.12–0.93; Table 5) in the Koum mudstones suggests a complex paleoclimatic history marked by fluctuations between arid and humid conditions. Paleosalinity (N values, Sr/Ba ratios) and paleoclimate (Sr/Cu, C-value) proxies (ESM_1; Table 5) indicate deposition in a dynamic environment with variable salinity, likely reflecting seasonal or long-term climatic changes. However, the presence of alteration minerals such as analcime, ankerite, and dolomite indicative of low-grade metamorphism and/or hydrothermal alteration suggests that these geochemical signatures may have been partially overprinted. Post-depositional processes are known to mobilize Sr and Cu, potentially altering the original Sr/Cu and Sr/Ba ratios. Strontium, for instance, can substitute into carbonates like dolomite and ankerite, leading to Sr enrichment during diagenesis or hydrothermal fluid interaction (Veizer 1983; Al-Aasm 2003; Cangelosi et al. 2020). In contrast, copper is more easily mobilized under oxidizing, acidic, or hydrothermal conditions, often resulting in its depletion (Chávez 2021). These alterations can artificially affect the Sr/Cu and Sr/Ba ratios, mimicking signals typical of arid or saline environments and biasing paleoclimate and paleosalinity interpretations. Thus, while the observed Sr/Cu and Sr/Ba trends suggest variable salinity and aridity, post-depositional modifications cannot be rolled out.

Tyson and Pearson (1991) defined four primary redox facies (oxic, dysoxic, suboxic, and anoxic) based on oxygen and hydrogen sulfide concentrations in aquatic environments. Algeo and Li (2020) further subdivided the suboxic facies into the suboxidized and subreduced categories. Redox environments can be characterized using various geochemical proxies, including those based on the C–S–Fe–P system (Raiswell et al. 1988; Poulton and Canfield 2011), such as Fe/Al ratios (Lyons and Severmann 2006) and $C_{org}/P = (TOC/12)/(P/30.97)$ ratios (Algeo and Ingall 2007), as well as those based on trace-metal enrichment factors (Algeo and Liu 2020), bimetallic ratios (Tang et al. 2020; Fathy et al. 2023), Ce anomalies (Tostevin et al. 2016), and biomarkers (Fathy et al. 2023).

Principal component analysis has shown that C–S–Fe–P system proxies and trace-metal enrichment factors are the most reliable indicators for paleoredox evaluations (Algeo and Liu 2020). While Ce anomalies can be informative, they may not be suitable for mudstones as they require a hydrogenous signal (Liu et al. 1988). The C_{org}/P ratio, a proxy from the C–S–Fe–P system, has been identified as a robust indicator of paleoredox conditions in recent studies (Wang et al. 2022; Lei et al. 2023). Given the brackish to saline nature of the Koum mudstones, the C_{org}/P ratio was selected for this study. Based on established C_{org}/P threshold values (oxic < 50, dysoxic/hypoxic 50–100, anoxic > 100) (Algeo and Ingall 2007), the wide range of C_{org}/P ratios (0.21 to 178.34; Table 5) for the Koum mudstones suggests that their depositional environment varied from oxic to anoxic conditions. This variability likely reflects changes in oxygen levels over time, potentially influenced by factors like water depth.

The Zr/Rb ratio is a proxy for inferring paleo-water depth and hydrodynamic conditions (Tang et al. 2020; Liu et al. 2020). Zirconium is preferentially concentrated in heavy minerals like zircon, typically found in shallow, high-energy environments. Rubidium, on the other hand, is enriched in light minerals such as clay, commonly deposited in deeper, low-energy settings (Ibach 1982; Dypvik and Harris 2001; Tenger et al. 2006). High Zr/Rb ratios indicate shallow, high-energy environments, while low ratios suggest deeper, low-energy environments (e.g., Omietimi et al. 2022; Wu et al. 2024). The low Zr/Rb ratios (0.07 to 0.49; ESM_1) for the Koum mudstones point to a deep-water, low-energy depositional environment.

5.3.3 *Constraints from $\delta^{13}C_{VPDB}$ composition*

The stable carbon isotope ratio, $\delta^{13}C$, offers a valuable tool for understanding past environments. By analyzing the carbon content of organic matter preserved in dark mudstones, we can reconstruct changes in climatic conditions over time (Gröcke 2002; Bocherens et al. 1993; Ratigan 2016). Plants utilize different photosynthetic pathways to fix carbon dioxide. C_3 plants (including angiosperms and conifers), the first photosynthetic land plants that date back to the Ordovician, use the Calvin–Benson cycle to directly fix CO_2 and thrive in cooler, temperate regions (Robinson and Hesselbo 1998). Their $\delta^{13}C$ values typically range from − 23 ‰ to − 34 ‰, with an average of − 27 ‰ (Gröcke 2002). In contrast, C_4 plants, adapted to warmer conditions, employ the Hatch–Slack pathway to fix CO_2 as oxaloacetate, leading to $\delta^{13}C$ values between − 8 ‰ and − 16 ‰, with an average of − 13 ‰ (Spicer and Parrish 1986; Gröcke 2002; Robinson and Hesselbo 2004).

While C_4 plants evolved in the Late Cretaceous, they only became ecologically significant around 6–7 Ma ago (Gröcke 2002; Ehleringer et al. 1991). Crassulacean acid metabolism (CAM) plants, a specialized group adapted to arid environments, emerged around 20–30 Ma ago (Keely and Rundel 2003). Their unique photosynthetic strategy allows them to conserve water, but their isotopic signature is less distinct and can overlap with C_3 and C_4 plants. In the Miocene, the $\delta^{13}C$ values for wood samples show angiosperms with values from − 24 ‰ to − 30 ‰, while conifers exhibit a range of − 19 ‰ to − 27 ‰, highlighting the potential to link shifts in $\delta^{13}C$ values to changes in ancient vegetation types (Poole and Bergen 2006). These distinct isotopic ranges can be used to infer vegetation types within carbon sources in geological records.

The average $\delta^{13}C$ values of the Koum mudstones (− 28.2 ‰; Table 4) is consistent with the $\delta^{13}C$ values from a terrestrial organic carbon source, primarily from C_3 plants (− 20 ‰ and − 34 ‰), which were dominant during the Cretaceous (Salazar-Jaramillo et al. 2016). The $\delta^{13}C$ values, plotted on a $\delta^{13}C_{VPDB}$ vs $\delta^{13}C$atm diagram, indicate a mix of organic matter source, including C_3 plants from temperate grasslands and cooler, forested environments (Arens et al. 2000; Fig. 12a). The slightly more negative $\delta^{13}C$ values (25.2 ‰ to − 35.2 ‰) for the Koum mudstones than expected for C_3 plants suggest potential influence from factors such as fluctuating CO_2 levels and mixing with marine carbon sources in continental or marginal marine settings (Bocherens et al. 1993; Gröcke 2002). Environmental factors such as CO_2 levels, salinity, and diagenetic alterations could

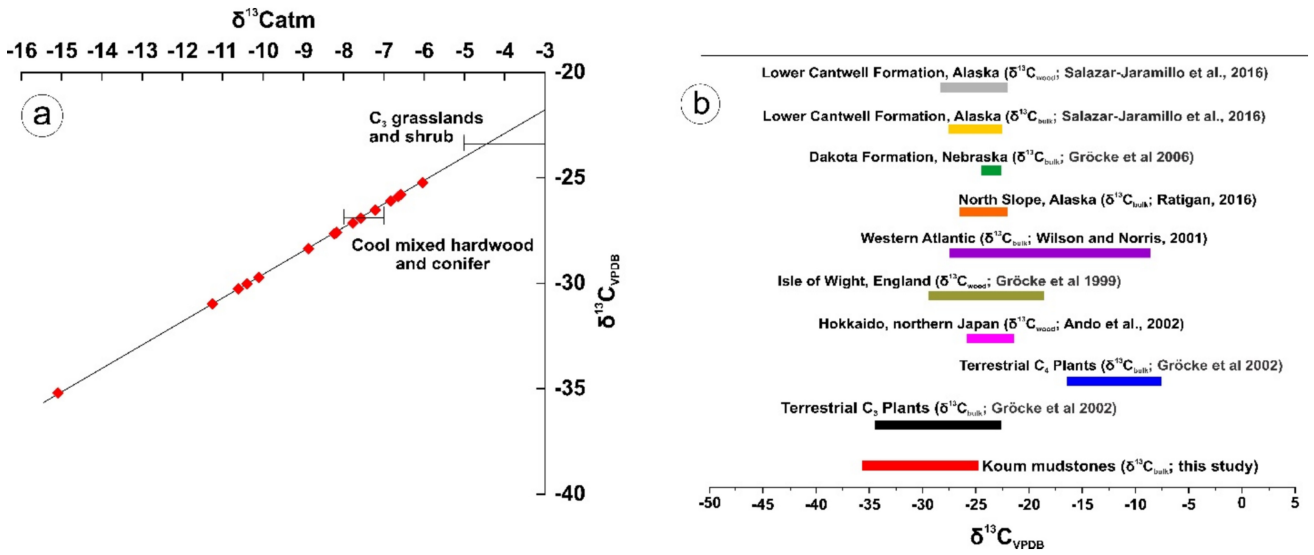

Fig. 12 Carbon isotope discrimination plots: **a** $\delta^{13}C$ versus $\delta^{13}C$atm (Arens et al. 2000), **b** $\delta^{13}C$ values for the Koum mudstones compared to global values

also have impacted the $\delta^{13}C$ values of the Koum mudstones (Naidu et al. 1993).

The $\delta^{13}C$ values of the Koum mudstones are broadly similar to global $\delta^{13}C$ trends during the Cretaceous (Fig. 12b). Although slightly more negative, the $\delta^{13}C$ values for the Koum mudstones are consistent with Aptian marine sediments from Hokkaido, Japan ($\delta^{13}C_{wood}$ values of − 25.4‰ to − 21.8‰), the Maastrichtian Cantwell Formation ($\delta^{13}C_{bulk}$ values of − 22.95‰ to − 27.10‰ and $\delta^{13}C_{wood}$ values of − 22.42‰ to − 27.85‰), the Cenomanian Dakota Formation of Nebraska ($\delta^{13}C_{bulk}$ values of − 24‰ to − 23‰), and the Cretaceous mudstones at Slope Mountain, Alaska ($\delta^{13}C_{bulk}$ of − 22. 5‰ to − 26.1‰), suggesting similar paleoenvironmental conditions with significant terrestrial C_3 plant input (Fig. 12b; Ando 2002; Gröcke et al. 2006; Salazar-Jaramillo et al. 2016; Ratigan 2016).

The comparatively more negative $\delta^{13}C$ excursions observed in the Koum mudstones, especially in the Kali sample KAL002 (− 35.2‰) and the Mayo Gaba samples KAL011 (− 30.0‰), KAL012 (− 29.7‰), and KAL013 (− 31.0‰) (Table 4), may be linked to fluctuations in atmospheric CO_2 levels or increased carbon burial events (Spicer and Parrish 1986; Naidu et al. 1993; Gröcke et al. 2002). These lower $\delta^{13}C$ values could indicate periods of reduced CO_2 or increased terrestrial organic matter input, potentially reflecting environmental stress. Overall, the $\delta^{13}C$ values of the Koum mudstones suggest a terrestrial, fluvial-deltaic environment with significant contributions from C_3 plants (Fig. 12b).

5.3.4 *Constraints from $\delta^{18}O_{VSMOW}$ and $\delta^{2}H_{VSMOW}$ composition*

Stable hydrogen and oxygen isotope ratios in clastic sediments are valuable tools for reconstructing past environmental and climatic conditions (e.g., Savin and Epstein 1970; Murray and Janssen 1984; Savin and Lee 1988; Santos et al. 2007). These isotopes, present in various water sources (e.g., connate water, seawater, meteoric water, organic water, metamorphic water, and igneous water), can significantly influence the isotopic composition of sediments (Morad et al. 2003; Middleton et al. 2015; Bauer et al. 2016; Xi et al. 2019).

Connate water is water trapped within sediments at the time of deposition. Seawater and meteoric water, with known isotopic compositions, are common reference standards. Seawater exhibits $\delta^{2}H$ and $\delta^{18}O$ values of 0‰ relative to the V-SMOW (Morad et al. 2003), while meteoric water exhibits $\delta^{2}H$ and $\delta^{18}O$ values that vary systematically with latitude and altitude, decreasing at higher latitudes and altitudes (Fig. 13). Evaporated seawater, formed through evaporation, undergoes a complex isotopic evolution, becoming

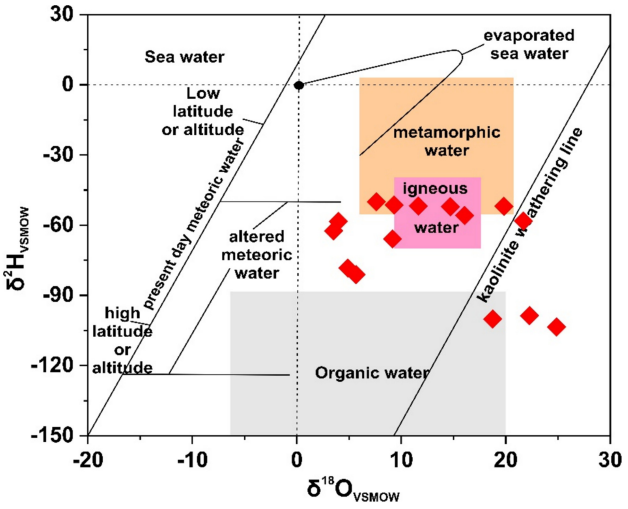

Fig. 13 Bivariate plot of $\delta^{18}O$ versus $\delta^{2}H$ values for the Koum mudstones, showing the different types of diagenetic fluids involved in their formation (Morad et al. 2003)

enriched in both $\delta^{18}O$ and $\delta^{2}H$, up to a salinity four times that of seawater (Fig. 13; Morad et al. 2003; Xi et al. 2019).

Organic water, formed through processes like kerogen maturation, microbial fermentation, and petroleum decomposition, has a wide range of isotopic signatures with $\delta^{2}H$ values typically ranging from − 150‰ to − 90‰, and $\delta^{18}O$ values varying from − 7‰ to 20‰ (Worden et al. 1996; Xi et al. 2019; Morad et al. 2003). In contrast, metamorphic and igneous fluids are generally enriched in $\delta^{18}O$ but depleted in $\delta^{2}H$ (Fig. 13). The $\delta^{18}O$ values for these waters range from 6‰ to 20 ‰ V-SMOW, while the $\delta^{2}H$ values vary from − 55‰ to 6‰ for metamorphic waters and − 70‰ to − 40‰ V-SMOW for igneous waters (Xi et al. 2019).

The $\delta^{18}O$ values of pore water in sedimentary basins are influenced by various factors during burial diagenesis, including changes in the geothermal gradient, hydration of volcanic materials, oil emplacement, mineral dissolution and precipitation, and fluid influx (Ayalon and Longstaffe 1988; Williams et al. 1997; Noh and Lee 1999; Marchand et al. 2002; Sample et al. 2017; Xi et al. 2019). Water–rock reactions and increased temperatures can lead to $\delta^{18}O$ enrichment, while meteoric water infiltration can gradually deplete $\delta^{18}O$ signatures (Haszeldine et al. 1992; Marchand et al. 2002). Additionally, the introduction of deep fluids can enrich pore water $\delta^{18}O$ signatures (Sample et al. 2017).

The wide range of $\delta^{18}O$ (3.6‰ to + 24.9‰) and $\delta^{2}H$ (− 104‰ to − 50‰) values for the Koum mudstones (Table 4) suggests interaction with different fluid sources, indicating variable climatic and hydrological conditions during deposition. The $\delta^{18}O$ values (+ 3.6‰ to + 24.9‰) suggest a provenance of chemically weathered intermediate igneous rock, with subsequent interaction with

magmatic–metamorphic and meteoric fluids (Table 4, Fig. 13).

Clastic sediments formed in high-latitude or high-altitude regions, where meteoric water is depleted in δ^2H and δ^{18}O signatures, typically indicate lower formation temperatures (Hassanipak and Eslinger 1985; Mizota and Longstaffe 1996). The average δ^2H (− 68 ‰; n = 15) and δ^{18}O (+ 12.2‰; n = 15) values for the Koum mudstones suggest a warm, equatorial-like climate during the Cretaceous, similar to the Cretaceous clays from the Lower Benue Trough of Nigeria, with average δ^2H and δ^{18}O values of − 59.66‰ and + 18.5‰, respectively (Bolarinwa et al. 2019). This contrasts with the more depleted average δ^2H (− 101.10‰) and δ^{18}O (+ 8.03‰) values observed in high-latitude regions, such as the eastern Australian clays (Bird and Chivas 1988).

In the δ^2H versus δ^{18}O diagram (Savin and Epstein 1970; Sheppard and Gilg 1996), the Koum mudstones largely cluster within or near the metamorphic and igneous fields, with some samples trending towards the altered meteoric water field (Fig. 13). The distribution of the samples is consistent with interactions involving magmatic, metamorphic and meteoric waters that has been isotopically modified (Fig. 13). The spread of some samples along the kaolinite weathering line hints at the influence of kaolinite formation, and weathering processes affecting the isotopic signatures (Fig. 13). The particularly low δ^2H values in the Mayo Gaba samples KAL011 (− 104‰), KAL012 (− 100‰), and KAL013 (− 99‰) (Table 4) may suggest prolonged exposure to meteoric water or mixing with fluids from a source with extremely low δ^2H signatures (Fig. 13).

The higher δ^{18}O values particularly in the Mayo Gaba samples KAL011 (+ 24.9‰) and KAL013 (+ 22.3‰) (Table 4) might indicate a stronger influence from deep, thermally altered fluids or prolonged burial diagenesis. The presence of certain minerals, such as analcine (1.9%–23.3%), ankerite (~ 10.5%) and dolomite (16.1%–19.8%) in some of the studied samples (Table 2; Fig. 4), further supports low-grade metamorphism and/or hydrothermal alteration. Overall, the variations in δ^{18}O and δ^2H values for the Koum mudstones suggest a complex history of hydrothermal, weathering, and possible diagenetic processes, involving meteoric fluids.

6 Tectonic setting of source area

The geochemical composition of mudstones can provide insights into the tectonic setting of their source areas. By analyzing major (e.g., K_2O, Na_2O, Al_2O_3, SiO_2) and trace elements (e.g., Th, La, Zr, Sc), we can distinguish between different tectonic settings (Roser and Korsch 1986; Sun et al. 2012; Bhatia 1983; Bhatia and Crook 1986; Pearce and Peate 1995; Verma and Armstrong-Altrin 2013; Wu et al. 2024). The geochemical data for the Koum mudstones, when plotted on the K_2O/Na_2O versus SiO_2 discrimination diagram after Roser and Korsch (1986), suggest a complex tectonic setting, likely involving active continental margin and island arc environments (Fig. 14a). However, on the SiO_2/Al_2O_3 vs. K_2O/Na_2O diagram of Maynard et al. (1982), most of the samples align with arc to active continental margin settings, with one sample suggesting a passive margin environment (Fig. 14b).

Trace element discrimination diagrams, such as the La versus Th and La-Th-Sc ternary diagrams of Bhatia and Crook (1986), are tools for determining the tectonic environment of source areas. When plotted on these diagrams, the Koum mudstones cluster near the fields associated with

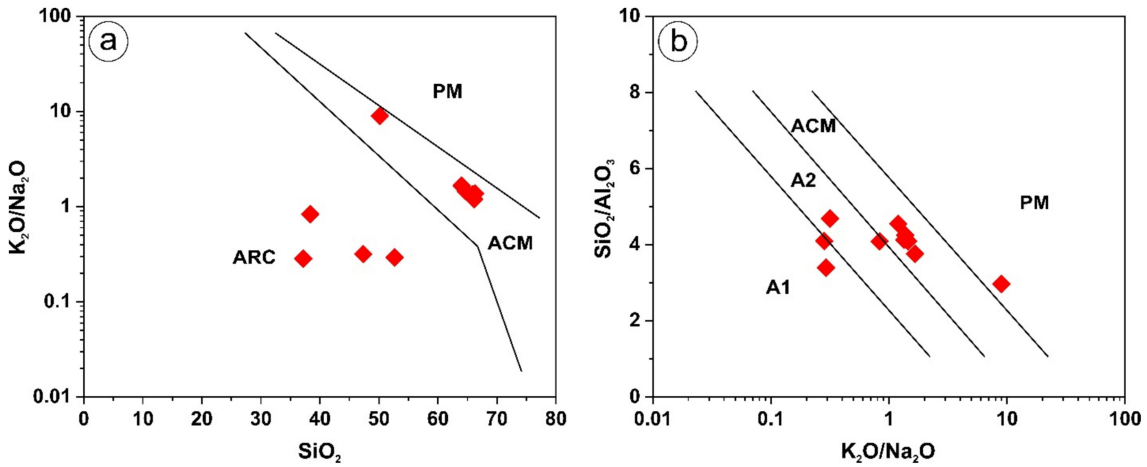

Fig. 14 Major element discrimination plots showing the tectonic setting of the Koum mudstones: **a** SiO_2 versus K_2O/Na_2O plot after Verma and Armstrong-Altrin (2013), and **b** K_2O/Na_2O versus SiO_2/Al_2O_3 plot after Maynard et al. (1982). *ACM* active continental margin, *ARC* island arc margin, *A1* arc, *A2* evolution arc, *PM* passive margin

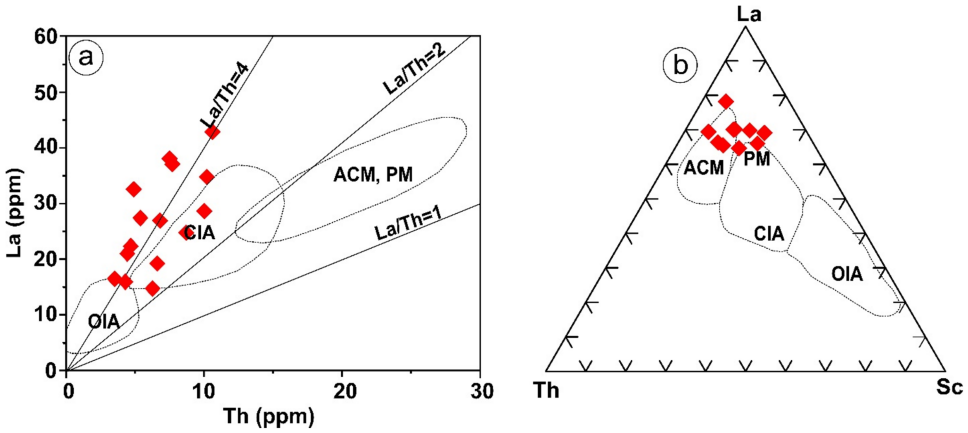

Fig. 15 Discrimination diagrams showing the tectonic setting of the Koum mudstones: **a** La versus Th plot after Bhatia and Crook (1986), and **b** La-Th-Sc diagram after Bhatia and Crook (1986). *ACM* active continental margin, *CIA* continental island arc, *OIA* oceanic island arc, *PM* passive continental margin

continental island arcs and ocean island arcs, suggesting an arc-related origin (Fig. 15a). However, the La-Th-Sc ternary diagram indicates an active continental margin (ACM) and a passive continental margin (PM) tectonic setting (Fig. 15b). These findings support a continental arc setting as the primary source for the Koum mudstones, with potential contributions from ocean island arc environments. This interpretation aligns with the findings of Ngo Mandeng et al. (2024a, b), who likewise proposed a continental arc system as the dominant source for the Koum basin deposits, with secondary contributions from rift and oceanic island arc systems.

7 Conclusions

This study presents the first integrated mineralogical, bulk-rock geochemical, and stable isotope (C–O–H) dataset for the Cretaceous dark-gray mudstones of the Koum Basin, northern Cameroon, providing new insights into the paleoenvironment, paleovegetation, paleoclimate, and tectonic evolution of this underexplored segment of the Upper Benue Trough. The following are some key findings of this study.

1. The mineralogical composition of the Koum mudstones indicates that they are predominantly composed of phyllosilicates, feldspars, carbonates, and minor iron oxides, reflecting a complex interplay of depositional processes and post-depositional alterations. The presence of alteration minerals such as analcime, dolomite, and ankerite suggests overprinting by low-grade metamorphism and/or hydrothermal activity.
2. Geochemically, the mudstones point to a continental crustal source with an intermediate igneous provenance, deposited in a dynamic basin environment characterized by fluctuations in salinity (brackish to saline), redox conditions (oxic to anoxic), and climatic conditions ranging from humid to arid. While the major element ratios (e.g., SiO_2 vs. $Al_2O_3 + K_2O + Na_2O$) indicate a dominant semi-arid regime, the Sr/Cu and C-values suggest alternating humid and arid conditions.
3. The $\delta^{13}C$ signatures for the mudstones suggest an organic carbon source, primarily from C_3 plants, indicative of a terrestrial, fluvial-deltaic environment. The slightly more negative $\delta^{13}C$ excursions exhibited by some samples reflect fluctuations in atmospheric CO_2 levels or increased terrestrial organic matter input.
4. The $\delta^{18}O$ and $\delta^{2}H$ values of the Koum mudstones suggest a complex history of fluid-rock interactions within the Koum basin, involving meteoric water and magmatic–metamorphic fluids under a warm, equatorial-like climate.
5. Tectonic setting discrimination diagrams suggest a continental arc environment for the Koum basin, with potential contributions from oceanic island arc and passive continental margin settings.

Acknowledgements The authors gratefully acknowledge the support of the Queen's Facility for Isotope Research (QFIR) for the isotopic and XRD analyses. We extend our sincere thanks to Ms. Evelyne Leduc for her invaluable assistance with communication and coordination. We also express our appreciation to Mr. Aurelien Temenou Tiolo and Mr. Kiven Paul Nsiidzeyu for their dedicated field assistance with sample collection.

Author contributions Nowel Yinkfu Njamnsi: writing–original draft, Methodology, Formal analysis, Data curation, Conceptualization, Resources; George Lemewihbwen Ngiamte: writing–review and editing, Methodology, Formal analysis, Data curation; Cheo Emmanuel Suh: writing–review and editing, Supervision, Conceptualization; Olivier Anoh Njoh: writing–review and editing, Supervision; Daniel Layton-Matthews: methodology, Formal analysis, Data curation; Peir Pufahl: methodology, Formal analysis, Data curation; Agatha Dobosz: methodology, Formal analysis, Data curation.

Declarations

Conflict of interests The authors declare that they have no known competing financial interests or personal relationships that could have appeared to influence the work reported in this paper.

References

Adatte T, Keller G, Stinnesbeck W (2002) Late Cretaceous to early Paleocene climate and sea-level fluctuations: the Tunisian record. Palaeogeogr Palaeoclimatol, Palaeoecol 178(3–4):165–196. https://doi.org/10.1016/S0031-0182(01)00395-9

Agbor-Taku J, Fon NN, Mbafor P, Bessong M, Njoh OA (2023a) Diagenesis, paleoenvironments, and petroleum geology of sediments lining the West and Central African Rift System, Koum Basin. North Cameroon Arab J Geosci 16(11):601. https://doi.org/10.1007/s12517-023-11710-9

Agbor-Taku J, Njoh OA, Fon NN, Bessong M (2023b) Sedimentology, T-R sequence stratigraphy and geochemical characterization of sedimentary successions of the West and Central African Rift System Koum Basin. Stratigraphy 20(4):303–333. https://doi.org/10.29041/strat.20.4.03

Agbor-Taku J, Njoh OA, Fon NN, Mbafor PU, Bessong M (2023c) A new lithostratigraphic profile for cretaceous to Paleogene successions in the west and central African rift system, Koum Basin, northern Cameroon. Stratigraphy 20(2):109–128. https://doi.org/10.29041/strat.20.2.02

Al-Aasm I (2003) Origin and characterization of hydrothermal dolomite in the western Canada sedimentary basin. J Geochem Explor 78:9–15. https://doi.org/10.1016/S0375-6742(03)00089-X

Algeo TJ, Ingall E (2007) Sedimentary Corg: P ratios, paleocean ventilation, and Phanerozoic atmospheric pO_2. Palaeogeogr Palaeoclimatol Palaeoecol 256(3–4):130–155. https://doi.org/10.1016/j.palaeo.2007.02.029

Algeo TJ, Li C (2020) Redox classification and calibration of redox thresholds in sedimentary systems. Geochim Cosmochim Acta 287:8–26. https://doi.org/10.1016/j.gca.2020.01.055

Algeo TJ, Liu JS (2020) A re-assessment of elemental proxies for paleoredox analysis. Chem Geol 540:119549. https://doi.org/10.1016/j.chemgeo.2020.119549

Ando A, Kakegawa T, Takashima R, Saito T (2002) New perspective on Aptian carbon isotope stratigraphy: Data from $\delta^{13}C$ records of terrestrial organic matter. Geology 30(3):227. https://doi.org/10.1130/0091-7613(2002)0300227:npoaci%3e2.0.co;2

Arens NC, Jahren AH, Amundson R (2000) Can C3 plants faithfully record the carbon isotopic composition of atmospheric carbon dioxide? Paleobiology 26(1):137–164. https://doi.org/10.1666/0094-8373(2000)026%3c0137:ccpfrt%3e2.0.co;2

Ayalon A, Longstaffe FJ (1988) Oxygen isotope studies of diagenesis and pore-water evolution in the western Canada sedimentary basin: evidence from the upper cretaceous basal belly river sandstone. Alberta SEPM J Sediment Res 58(3):489–505. https://doi.org/10.1306/212f8dcd-2b24-11d7-8648000102c1865d

Bauer KK, Vennemann TW, Gilg HA (2016) Stable isotope composition of bentonites from the Swiss and Bavarian Freshwater Molasse as a proxy for paleoprecipitation. Palaeogeogr Palaeoclimatol Palaeoecol 455:53–64. https://doi.org/10.1016/j.palaeo.2016.02.002

Bauluz B, Mayayo MJ, Fernandez-Nieto C, Gonzalez Lopez JM (2000) Geochemistry of Precambrian and Paleozoic siliciclastic rocks from the Iberian range (NE Spain): Implications for source-area weathering, sorting, provenance, and tectonic setting. Chem Geol 168(1–2):135–150. https://doi.org/10.1016/S0009-2541(00)00192-3

Berner RA, Kothavala Z (2001) GEOCARB III: a revised model of atmospheric CO_2 over Phanerozoic time. Am J Sci 301(2):182–204. https://doi.org/10.2475/ajs.301.2.182

Bessong M, Hell JV, Samankassou E, Feist-Burkhardt S, Eyong JT, Ngos S, Nolla JD, Mbesse CO, Adatte T, Mfoumbeng MP, Dissombo EAN, Ntsama AJ, Mouloud B, Ndjeng E (2018) Hydrocarbon potential, palynology and palynofacies of four sedimentary basins in the Benue Trough, northern Cameroon. J Afr Earth Sci 139:73–95. https://doi.org/10.1016/j.jafrearsci.2017.11.012

Bhatia MR (1983) Plate tectonics and geochemical composition of sandstones. J Geol 91(6):611–627. https://doi.org/10.1086/628815

Bhatia MR, Crook KAW (1986) Trace element characteristics of graywackes and tectonic setting discrimination of sedimentary basins. Contrib Mineral Petrol 92(2):181–193. https://doi.org/10.1007/BF00375292

Bice KL, Norris RD (2002) Possible atmospheric CO_2 extremes of the middle cretaceous (late Albian–Turonian). Paleoceanography 17(4):1070. https://doi.org/10.1029/2002pa000778

Bice KL, Birgel D, Meyers PA, Dahl KA, Hinrichs KU, Norris RD (2006) A multiple proxy and model study of Cretaceous upper ocean temperatures and atmospheric CO_2 concentrations. Paleoceanography. https://doi.org/10.1029/2005pa001203

Bird MI, Chivas AR (1988) Stable-isotope evidence for low-temperature kaolinitic weathering and post-formational hydrogen-isotope exchange in Permian kaolinites. Chem Geol Isot Geosci Sect 72(3):249–265. https://doi.org/10.1016/0168-9622(88)90028-0

Bocherens H, Friis EM, Mariotti A, Pedersen KR (1993) Carbon isotopic abundances in Mesozoic and Cenozoic fossil plants: Palaeoecological implications. Lethaia 26(4):347–358. https://doi.org/10.1111/j.1502-3931.1993.tb01541.x

Bolarinwa AT, Faloye O, Idakwo SO (2022) Geochemical studies of shales from the Asu River Group, Lower Benue Trough: implications for provenance and paleo-environment reconstruction. Solid Earth Sci 7(1):5–18. https://doi.org/10.1016/j.sesci.2021.12.002

Boutton TW, Nordt L, Archer SR, Midwood AJ, and Casar I (1993) Stable carbon isotope ratios of soil organic matter and their potential use as indicators of palaeoclimate.

Bristow TF, Kennedy MJ, Derkowski A, Droser ML, Jiang GQ, Creaser RA (2009) Mineralogical constraints on the paleoenvironments of the Ediacaran Doushantuo formation. Proc Natl Acad Sci USA 106(32):13190–13195. https://doi.org/10.1073/pnas.0901080106

Brunet M, Coppens Y, Dejax J, Flynn L, Heintz E, Hell J, Jacobs L, Jehenne Y, Mouchelin G, Pilbeam D, Sudre J (1990) Nouveaux mammifères du Crétacé inférieur du Cameroun, Afrique de l'Ouest. Comptes Rendus De L'académie des Sciences De Paris, Série 310:1139–1146

Campbell C, Heapes S (2008) An atlas of oil and gas depletion. Jeremy Mills Publishing, Huddersfield, Reino Unido

Cangelosi D, Broom-Fendley S, Banks D, Morgan D, Yardley B (2020) Light rare earth element redistribution during hydrothermal alteration at the Okorusu carbonatite complex. Namibia Minmag 84(1):49–64. https://doi.org/10.1180/mgm.2019.54

Cao J, Wu M, Chen Y, Hu K, Bian LZ, Wang LG, Zhang Y (2012) Trace and rare earth element geochemistry of Jurassic mudstones in the northern Qaidam Basin, northwest China. Geochemistry 72(3):245–252. https://doi.org/10.1016/j.chemer.2011.12.002

Chaboureau AC, Guillocheau F, Robin C, Rohais S, Moulin M, Aslanian D (2013) Paleogeographic evolution of the central segment of the South Atlantic during Early Cretaceous times: paleotopographic and geodynamic implications. Tectonophysics 604:191–223. https://doi.org/10.1016/j.tecto.2012.08.025

Chamley H (1989) Clay sedimentology. Springer-Verlag, Berlin, p 623

Charbonnier G, Duchamp-Alphonse S, Deconinck JF, Adatte T, Spangenberg JE, Colin C, Föllmi KB (2020) A global Palaeoclimatic reconstruction for the Valanginian based on clay mineralogical and geochemical data. Earth Sci Rev 202:103092. https://doi.org/10.1016/j.earscirev.2020.103092

Chávez WX Jr (2021) Weathering of copper deposits and copper mobility: mineralogy, geochemical stratigraphy, and exploration

implications. SEG Newslett 126:16–27. https://doi.org/10.5382/segnews.2021-126.fea-01

Chen J, Qian H, Gao YY, Wang HK, Zhang MS (2020) Insights into hydrological and hydrochemical processes in response to water replenishment for lakes in arid regions. J Hydrol 581:124386. https://doi.org/10.1016/j.jhydrol.2019.124386

Chen H, Tang DZ, Chen SD, Tang SL (2022) Geochemical characteristics of mudstones from the lower Cretaceous strata of the Jixi Basin, NE China: implications for organic matter enrichment. Int J Coal Geol 249:103904. https://doi.org/10.1016/j.coal.2021.103904

Cojan I, Moreau MG, Stott LE (2000) Stable carbon isotope stratigraphy of the Paleogene pedogenic series of southern France as a basis for continental-marine correlation. Geology 28(3):259. https://doi.org/10.1130/0091-7613(2000)28%3c259:scisot%3e2.0.co;2

Condie KC (1993) Chemical composition and evolution of the upper continental crust: contrasting results from surface samples and shales. Chem Geol 104(1–4):1–37. https://doi.org/10.1016/0009-2541(93)90140-E

Congleton JD, Flynn LJ, Jacobs LL, Brunet M, Dejax J, Hell J, Pilbeam D (1992) Preliminary correlation of continental sediments of the Koum Basin, northern Cameroon. In: eds. Mateer NJ, Chen PJ Aspects of nonmarine Cretaceous geology. China Ocean Press, Beijing. pp 213–219.

Congleton JD (1990) Vertebrate paleontology of the Koum Basin, northern Cameroon, and archosaurian paleobiogeography in the Early Cretaceous (PhD dissertation). Southern Methodist University.

Cox R, Lowe DR, Cullers RL (1995) The influence of sediment recycling and basement composition on evolution of mudrock chemistry in the southwestern United States. Geochim Cosmochim Acta 59(14):2919–2940. https://doi.org/10.1016/0016-7037(95)00185-9

Cullers RL, Basu A, Suttner LJ (1988) Geochemical signature of provenance in sand-size material in soils and stream sediments near the Tobacco Root batholith, Montana, USA. Chem Geol 70(4):335–348. https://doi.org/10.1016/0009-2541(88)90123-4

Dawson D, Grice K, Wang SX, Alexander R, Radke J (2004) Stable hydrogen isotopic composition of hydrocarbons in torbanites (Late Carboniferous to Late Permian) deposited under various climatic conditions. Org Geochem 35(2):189–197. https://doi.org/10.1016/j.orggeochem.2003.09.004

Deconinck JF, Hesselbo SP, Debuisser N, Averbuch O, Baudin F, Bessa J (2003) Environmental controls on clay mineralogy of an Early Jurassic mudrock (Blue Lias Formation, southern England). Int J Earth Sci 92(2):255–266. https://doi.org/10.1007/s00531-003-0318-y

Deconinck JF, Hesselbo SP, Pellenard P (2019) Climatic and sea-level control of Jurassic (Pliensbachian) clay mineral sedimentation in the Cardigan Bay Basin, Llanbedr (Mochras Farm) borehole. Wales Sedimentology 66(7):2769–2783. https://doi.org/10.1111/sed.12610

Deconinck JF, Gómez JJ, Baudin F, Biscay H, Bruneau L, Cocquerez T, Mathieu O, Pellenard P, Santoni AL (2020) Diagenetic and environmental control of the clay mineralogy, organic matter and stable isotopes (C, O) of Jurassic (Pliensbachian-lowermost Toarcian) sediments of the Rodiles section (Asturian Basin, Northern Spain). Mar Petrol Geol 115:104286. https://doi.org/10.1016/j.marpetgeo.2020.104286

Dejax J, Michard JG, Brunet M, Hell J (1989) Dinosaur footprints from the Lower Cretaceous of the Babouri-Figuil basin (Bénoué graben, Cameroon). Neues Jahrbuch für Geologie und Paläontologie. Abhandlungen 178(1):85–108. https://doi.org/10.1127/njgpa/178/1989/85

Di Muzio T, Ovadia JS (2006) Energy, capitalism and world order: toward a new agenda in international political economy. Palgrave Macmillan, Basingstoke

Dou LR, Xiao KY, Wang JC (2023) Regional geological characteristics of the central African Rift system. Petroleum Geology and Exploration of the Bongor Basin. Springer Nature Singapore, pp 25–67. https://doi.org/10.1007/978-981-19-2673-0_2

Dudek T (2012) Clay minerals as Palaeoenvironmental indicators in the Bathonian (Middle Jurassic) ore-bearing clays from Gnaszyn. Kraków-Silesia Homocline Acta Geol Pol 62(3):297–305. https://doi.org/10.2478/v10263-012-0016-9

Dutta PK, Suttner LJ (1986) Alluvial sandstone composition and paleoclimate; II, Authigenic mineralogy. J Sediment Res 56(3):346–358. https://doi.org/10.1306/212f8909-2b24-11d7-8648000102c1865d

Dypvik H, Harris NB (2001) Geochemical facies analysis of fine-grained siliciclastics using Th/U, Zr/Rb and (Zr+Rb)/Sr ratios. Chem Geol 181(1–4):131–146. https://doi.org/10.1016/S0009-2541(01)00278-9

Ehleringer JR, Sage RF, Flanagan LB, Pearcy RW (1991) Climate change and the evolution of C_4 photosynthesis. Trends Ecol Evol 6(3):95–99. https://doi.org/10.1016/0169-5347(91)90183-X

Fagel N (2007) Chapter four: Clay minerals, deep circulation and climate. In: HillaireMarcel C and De Vernal A eds Proxies in Late Cenozoic Paleoceanography, Developments in marine geology (1st ed.) Elsevier. pp 139–184. https://doi.org/10.1016/s1572-5480(07)01009-3

Fairhead JD (2020) Chapter 20: regional tectonics and basin formation: the role of potential field studies–an application to the Mesozoic West and Central African Rift System. Reg Geol Tectonics. https://doi.org/10.1016/B978-0-444-64134-2.00018-3

Fairhead JD (2009) The Mesozoic west and central African rift system: Qualitative evaluation. Search and Discovery Article #30077 (2009) Adapted from oral presentation at AAPG International conference and exhibition, Cape Town, South Africa. October 26–29, 2008.

Fathy D, Wagreich M, Fathi E, Ahmed MS, Leila M, Sami M (2023) Maastrichtian anoxia and its influence on organic matter and trace metal patterns in the southern Tethys realm of Egypt during greenhouse variability. ACS Omega 8(22):19603–19612. https://doi.org/10.1021/acsomega.3c01096

Fedo CM, Wayne Nesbitt H, Young GM (1995) Unraveling the effects of potassium metasomatism in sedimentary rocks and paleosols, with implications for paleoweathering conditions and provenance. Geology 23(10):921–924. https://doi.org/10.1130/0091-7613(1995)023%3c0921:uteopm%3e2.3.co;2

Floyd PA, Leveridge BE (1987) Tectonic environment of the Devonian Gramscatho basin, south Cornwall: Framework mode and geochemical evidence from turbiditic sandstones. J Geol Soc 144(4):531–542. https://doi.org/10.1144/gsjgs.144.4.0531

Genik GJ (1992) Regional framework, structural and petroleum aspects of rift basins in Niger, chad and the central African Republic (CAR). Tectonophysics 213(1–2):169–185. https://doi.org/10.1016/0040-1951(92)90257-7

Genik GJ (1993) Petroleum geology of cretaceous-tertiary Rift basins in Niger, Chad, and central African republic. AAPG Bull 77(8):1405–1434. https://doi.org/10.1306/bdff8eac-1718-11d7-8645000102c1865d

Gertsch B, Keller G, Adatte T, Garg R, Prasad V, Berner Z, Fleitmann D (2011) Environmental effects of Deccan volcanism across the Cretaceous–tertiary transition in Meghalaya. India Earth Planet Sci Lett 310(3–4):272–285. https://doi.org/10.1016/j.epsl.2011.08.015

Ghasemian S, Faridzad A, Abbaszadeh P, Taklif A, Ghasemi A, Hafezi R (2020) An overview of global energy scenarios by

2040: Identifying the driving forces using cross-impact analysis method. Int J Environ Sci Technol 21(11):7749–7772. https://doi.org/10.1007/s13762-020-02738-5

Girty GH, Ridge DL, Knaack C, Johnson D, Al-Riyami RK (1996) Provenance and depositional setting of Paleozoic chert and argillite, Sierra Nevada. California SEPM J Sediment Res 66(1):107–118. https://doi.org/10.1306/d42682ca-2b26-11d7-8648000102c1865d

Graham E, Ovadia JS (2019) Oil exploration and production in sub-Saharan Africa, 1990-present: trends and developments. Extr Ind Soc 6(2):593–609. https://doi.org/10.1016/j.exis.2019.02.001

Grocke DR (2002) The carbon isotope composition of ancient CO_2 based on higher-plant organic matter. Philos Trans R Soc Lond Ser A Math Phys Eng Sci 360(1793):633–658. https://doi.org/10.1098/rsta.2001.0965

Gröcke DR, Ludvigson GA, Witzke BL, Robinson SA, Joeckel RM, Ufnar DF, Ravn RL (2006) Recognizing the Albian-Cenomanian (OAE1d) sequence boundary using plant carbon isotopes: Dakota Formation, Western Interior Basin, USA. Geology 34(3):193. https://doi.org/10.1130/g21998.1

Guiraud R, Maurin JC (1992) Early cretaceous rifts of western and central Africa: an overview. Tectonophysics 213(1–2):153–168. https://doi.org/10.1016/0040-1951(92)90256-6

Hallam A, Grose JA, Ruffell AH (1991) Palaeoclimatic significance of changes in clay mineralogy across the Jurassic-Cretaceous boundary in England and France. Palaeogeogr Palaeoclimatol Palaeoecol 81(3–4):173–187. https://doi.org/10.1016/0031-0182(91)90146-I

Harris NB, Freeman KH, Pancost RD, White TS, Mitchell GD (2004) The character and origin of lacustrine source rocks in the Lower Cretaceous synrift section, Congo Basin, west Africa. AAPG Bull 88(8):1163–1184. https://doi.org/10.1306/02260403069

Hassanipak AA, Eslinger E (1985) Mineralogy, crystallinity, O^{18}/O^{16}, and D/H of Georgia kaolins. Clays Clay Miner 33(2):99–106. https://doi.org/10.1346/ccmn.1985.0330203

Haszeldine RS, Brint JF, Fallick AE, Hamilton PJ, Brown S (1992) Open and restricted hydrologies in Brent group diagenesis: North Sea. Geol Soc Lond Spec Publ 61(1):401–419. https://doi.org/10.1144/gsl.sp.1992.061.01.20

Hayashi KI, Fujisawa H, Holland HD, Ohmoto H (1997) Geochemistry of ~1.9 Ga sedimentary rocks from northeastern Labrador, Canada. Geochim Cosmochim Acta 61(19):4115–4137. https://doi.org/10.1016/S0016-7037(97)00214-7

Herron MM (1988) Geochemical classification of terrigenous sands and shales from core or log data. SEPM J Sediment Res 58(5):820–829. https://doi.org/10.1306/212f8e77-2b24-11d7-8648000102c1865d

Höök M, Hirsch R, Aleklett K (2009) Giant oil field decline rates and their influence on world oil production. Energy Policy 37(6):2262–2272. https://doi.org/10.1016/j.enpol.2009.02.020

Hu XF, Liu QJ, Liu R, Sun PC, Hu SC, Meng QT, Liu SY (2012) Clay mineral and inorganic geochemical characteristics of Eocene Huadian Formation in Huadian Basin and their paleoenvironment implications. J China Coal Soc 37(3):416–423

Hu JJ, Li Q, Song CY, Wang SQ, Shen B (2017) Geochemical characteristics of the Permian sedimentary rocks from Qiangtang basin: constraints for paleoenvironment and paleoclimate. Terr Atmos Ocean Sci 28(3):271–282. https://doi.org/10.3319/tao.2016.08.08.01

Huber BT, Norris RD, MacLeod KG (2002) Deep-sea paleotemperature record of extreme warmth during the Cretaceous. Geology 30(2):123–126. https://doi.org/10.1130/0091-7613(2002)030%3c0123:DSPROE%3e2.0.CO;2

Ibach LEJ (1982) Relationship between sedimentation rate and total organic carbon content in ancient marine sediments. AAPG Bull 66(2):170–188. https://doi.org/10.1306/03b59a5d-16d1-11d7-8645000102c1865d

Jacobs LL, Winkler DA, Gomani EM (1996) Cretaceous dinosaurs of Africa: examples from Cameroon and Malawi. Mem Que Mus 39(3):595–610

Jia JL, Liu ZJ, Bechtel A, Strobl SAI, Sun PC (2013) Tectonic and climate control of oil shale deposition in the upper cretaceous Qingshankou formation (Songliao Basin, NE China). Int J Earth Sci 102(6):1717–1734. https://doi.org/10.1007/s00531-013-0903-7

Keeley JE, Rundel PW (2003) Evolution of CAM and C_4 carbon-concentrating mechanisms. Int J Plant Sci 164(S3):S55–S77. https://doi.org/10.1086/374192

Kuypers MMM, Pancost RD, Damsté JSS (1999) A large and abrupt fall in atmospheric CO_2 concentration during cretaceous times. Nature 399(6734):342–345. https://doi.org/10.1038/20659

Lambiase JJ (1990) A model for tectonic control of lacustrine stratigraphic sequences in continental rift basins. In: Katz BJ ed. Lacustrine basin exploration: Case studies and modern analogs. pp 265–276. https://doi.org/10.1306/m50523c16

Lanson B, Sakharov BA, Claret F, Drits VA (2009) Diagenetic smectite-to-illite transition in clay-rich sediments: a reappraisal of X-ray diffraction results using the multi-specimen method. Am J Sci 309(6):476–516. https://doi.org/10.2475/06.2009.03

Latham A (2019) Exploration update and global fiscal terms. In: Proceedings of the 2019 South East Asia Petroleum Exploration Society (SEAPEX) Conference. Southeast Asia Petroleum Exploration Society, p. 2

Lawson M, Formolo MJ, Summa L, Eiler JM (2018) Geochemical applications in petroleum systems analysis: New constraints and the power of integration. Geol Soc Lond Spec Publ 468(1):1–21. https://doi.org/10.1144/sp468.6

Lei W, Chen D, Liu Z, Cheng M (2023) Paleoenvironment-driven organic matter accumulation in lacustrine shale mixed with shell bioclasts: A case study from the Jurassic Da'anzhai member, Sichuan Basin (China). J Pet Sci Eng 220:111178

Leng MJ, Marshall JD (2004) Palaeoclimate interpretation of stable isotope data from lake sediment archives. Quat Sci Rev 23(7–8):811–831. https://doi.org/10.1016/j.quascirev.2003.06.012

Lentini MR, Fraser SI, Sumner HS, Davies RJ (2010) Geodynamics of the central south Atlantic conjugate margins: Implications for hydrocarbon potential. Petrol Geosci 16(3):217–229. https://doi.org/10.1144/1354-079309-909

Lerman A (1978) Lakes: chemistry, geology, physics. Springer, New York. https://doi.org/10.1007/978-1-4757-1152-3

Lerman A, Imboden DM, Gat JR, Chou L (1995) Physics and chemistry of lakes. Springer-Verlag, Berlin

Li C, Yang S (2010) Is chemical index of alteration (CIA) a reliable proxy for chemical weathering in global drainage basins? Am J Sci 310(2):111–127. https://doi.org/10.2475/02.2010.03

Li C, Lightfoot PC, Amelin Y, Naldrett AJ (2000) Contrasting petrological and geochemical relationships in theVoisey's bay and mushuau intrusions, Labrador, Canada: Implications for OreGenesis. Econ Geol 95(4):771–799. https://doi.org/10.2113/gsecongeo.95.4.771

Litvinenko V (2020) The role of hydrocarbons in the global energy agenda: the focus on liquefied natural gas. Resources 9(5):59. https://doi.org/10.3390/resources9050059

Liu YJ, Huang CY, Zhou YQ, Lu YC, Ma Q (2020) The controlling factors of lacustrine shale lithofacies in the Upper Yangtze Platform (South China) using artificial neural networks. Mar Petrol Geol 118:104350. https://doi.org/10.1016/j.marpetgeo.2020.104350

López JMG, Bauluz B, Fernández-Nieto C, Oliete AY (2005) Factors controlling the trace-element distribution in fine-grained rocks:

the Albian kaolinite-rich deposits of the Oliete Basin (NE Spain). *Chemical Geology, 214*(1–2), 1–19

Maurin JC, Benkhelil J, Robineau B (1986) Wrench tectonics in Upper Benue. In NE Nigeria: influence on the Cretaceous Benue Trough. 13ème Colloque de Géologie Africaine, ST Andrews, 199

Maynard JB, Valloni R, Yu HS (1982) Composition of modern deep-sea sands from arc-related basins. Geol Soc Lond Spec Publ 10(1):551–561. https://doi.org/10.1144/gsl.sp.1982.010.01.36

McDonough WF, Sun SS (1995) The composition of the Earth. Chem Geol 120(3–4):223–253. https://doi.org/10.1016/0009-2541(94)00140-4

McLennan SM (2001) Relationships between the trace element composition of sedimentary rocks and upper continental crust. Geochem Geophys Geosyst. https://doi.org/10.1029/2000gc000109

McLennan SM, Taylor SR (1991) Sedimentary rocks and crustal evolution: Tectonic setting and secular trends. J Geol 99(1):1–21. https://doi.org/10.1086/629470

McLennan SM, McCulloch MT, Taylor SR, Maynard JB (1989) Effects of sedimentary sorting on neodymium isotopes in deep-sea turbidites. Nature 337(6207):547–549. https://doi.org/10.1038/337547a0

McLennan SM, Hemming S, McDaniel DK, Hanson GN (1993) Geochemical approaches to sedimentation, provenance, and tectonics. In: Johnsson MJ, Basu A eds Processes controlling the composition of clastic sediments. pp 21–40. https://doi.org/10.1130/spe284-p21

Meng QT, Liu ZJ, Bruch AA, Liu R, Hu F (2012) Palaeoclimatic evolution during Eocene and its influence on oil shale mineralisation, Fushun basin, China. J Asian Earth Sci 45:95–105. https://doi.org/10.1016/j.jseaes.2011.09.021

Meunier A, Caner L, Hubert F, El Albani A, Pret D (2013) The weathering intensity scale (WIS): an alternative approach of the chemical index of alteration (CIA). Am J Sci 313(2):113–143. https://doi.org/10.2475/02.2013.03

Middleton AW, Uysal IT, Golding SD (2015) Chemical and mineralogical characterisation of illite–smectite: implications for episodic tectonism and associated fluid flow, central Australia. Geochim Cosmochim Acta 148:284–303. https://doi.org/10.1016/j.gca.2014.09.035

Mimba ME, Ohba T, Nguemhe Fils SC, Nforba MT, Numanami N, Bafon TG, Aka FT, Suh CE (2018) Regional geochemical baseline concentration of potentially toxic trace metals in the mineralized Lom Basin, East Cameroon: a tool for contamination assessment. Geochem Trans 19(1):11. https://doi.org/10.1186/s12932-018-0056-5

Mizota C, Longstaffe FJ (1996) Origin of Cretaceous and Oligocene kaolinites from the iwaizumi clay deposit, iwate, northeastern Japan. Clays Clay Miner 44(3):408–416. https://doi.org/10.1346/CCMN.1996.0440310

Moore DM, Reynolds RC (1997) X-ray diffraction and the identification and analysis of clay minerals: 2nd edition. Oxford University Press, New York, NY, pp 378.

Morad S, Worden R, Ketzer J (2003) Oxygen and hydrogen isotopic composition of diagenetic clay minerals in sandstones: a review of the data and controls. Int Assoc Sedimentol Spec Publ 34:63–91

Moradi AV, Sarı A, Akkaya P (2016) Geochemistry of the Miocene oil shale (Hançili Formation) in the Çankırı-Çorum Basin, central Turkey: implications for paleoclimate conditions, source–area weathering, provenance and tectonic setting. Sediment Geol 341:289–303. https://doi.org/10.1016/j.sedgeo.2016.05.002

Morley CK (1999) Comparison of hydrocarbon prospectivity in rift systems. In: ed. CK Morley Continental rifting in East Africa, structural and sedimentary geometries, processes and evolution: as revealed by hydrocarbon exploration. American Association of Petroleum Geologists Special Publication

Murray HH, Janssen J (1984) Oxygen isotopes–indicators of kaolin genesis. Proc. 27th Int Geol Congr 15:287–303

Naidu AS, Scalan RS, Feder HM, Goering JJ, Hameedi MJ, Parker PL, Behrens EW, Caughey ME, Jewett SC (1993) Stable organic carbon isotopes in sediments of the north Bering-south Chukchi seas. Alaskan-Soviet Arctic Shelf Cont Shelf Res 13(5–6):669–691. https://doi.org/10.1016/0278-4343(93)90099-J

Nesbitt HW, Young GM (1982) Early Proterozoic climates and plate motions inferred from major element chemistry of lutites. Nature 299:715–717. https://doi.org/10.1038/299715a0

Nesbitt HW, Young GM (1989) Formation and diagenesis of weathering profiles. J Geol 97(2):129–147. https://doi.org/10.1086/629290

Ngo Mandeng G, Boboye OA, Bessong M, Mbabi Bitchong A (2024a) Maastrichtian-Paleocene environmental and climatic conditions in Koum Basin (northern Benue Trough, Cameroon) inferred using a multiproxy approach including sedimentology, mineralogy, and geochemistry. J Afr Earth Sci 209:105129. https://doi.org/10.1016/j.jafrearsci.2023.105129

Ngo Mandeng G, Boboye OA, Bessong M, Mbabi Bitchong A, Adatte T (2024b) Mineralogical evolution and Cretaceous paleoclimate inferences in the central Koum Basin. North Cameroon J Earth Syst Sci 133(3):149. https://doi.org/10.1007/s12040-024-02361-9

Njamnsi NY, Anoh NO, Lemewihbwen GN, Suh CE, Tamfu SF (2022a) Molecular organic geochemistry of mudstones from Koum Basin, Cameroon: paleo-environmental, age, maturity, and genetic implication. J Geosci 10(1):45–64. https://doi.org/10.12691/jgg-10-1-4

Njamnsi NY, Njoh OA, Ngiamte GL, Ndengwe AT, Suh CE, Tamfu SF (2022b) Optical and geochemical assessment of petroleum source rock potential and Palaeodepositional environments of Cretaceous mudstones, Koum Basin. North Cameroon J Afr Earth Sci 196:104674. https://doi.org/10.1016/j.jafrearsci.2022.104674

Noh JH, Lee I (1999) Diagenetic pore fluid evolution in the Pohang Miocene sediments: oxygen isotopic evidence of septarian carbonate concretions and authigenic mineral phases. Geosci J 3(3):141–149. https://doi.org/10.1007/BF02910270

Nolla JD, Hell JV, Ngos S III, Bessong M, Mfoumbeng MP, Eyong Takem J, Dissombo Edimo AN, Mbang AR, Engombi G, Ndjeng E (2015) Lithostratigraphy of the Koum Basin (Northern Cameroon). Int J Multidiscip Res Dev 2(6):103–114

Nwachukwu JI (1985) Petroleum prospects of Benue trough. Nigeria AAPG Bulletin 69(4):601–609. https://doi.org/10.1306/ad46253d-16f7-11d7-8645000102c1865d

Omietimi EJ, Lenhardt N, Yang RC, Götz AE, Bumby AJ (2022) Sedimentary geochemistry of Late Cretaceous-Paleocene deposits at the southwestern margin of the Anambra Basin (Nigeria): implications for paleoenvironmental reconstructions. Palaeogeogr Palaeoclimatol Palaeoecol 600:111059. https://doi.org/10.1016/j.palaeo.2022.111059

Partin CA, Lalonde SV, Planavsky NJ, Bekker A, Rouxel OJ, Lyons TW, Konhauser KO (2013) Uranium in iron formations and the rise of atmospheric oxygen. Chem Geol 362:82–90. https://doi.org/10.1016/j.chemgeo.2013.09.005

Pearce JA, Peate DW (1995) Tectonic implications of the composition of volcanic arc magmas. Annu Rev Earth Planet Sci 23:251–286. https://doi.org/10.1146/annurev.ea.23.050195.001343

Peng Q, Chongyi E, Li XZ, Sun YJ, Zhang J, Zhang SQ, Shi YK, Ji XB, Zhang ZK (2024) Holocene paleoclimate changes around Qinghai Lake in the northeastern Qinghai-Tibet Plateau: Insights from isotope geochemistry of aeolian sediment. Atmosphere 15(7):833. https://doi.org/10.3390/atmos15070833

Petters SW, Ekweozor CM (1982) Petroleum geology of Benue Trough and southeastern Chad Basin, Nigeria: Geologic notes. AAPG Bull 66(8):1141–1149. https://doi.org/10.1306/03b5a65b-16d1-11d7-8645000102c1865d

Poole I, van Bergen PF (2006) Physiognomic and chemical characters in wood as Palaeoclimate proxies. Plants and Climate Change. Springer Netherlands, pp 175–196. https://doi.org/10.1007/978-1-4020-4443-4_12

Poulton SW, Canfield DE (2011) Ferruginous conditions: a dominant feature of the ocean through Earth's history. Elements 7(2):107–112. https://doi.org/10.2113/gselements.7.2.107

Price JR, Velbel MA (2003) Chemical weathering indices applied to weathering profiles developed on heterogeneous felsic metamorphic parent rocks. Chem Geol 202(3–4):397–416. https://doi.org/10.1016/j.chemgeo.2002.11.001

Qu CS, Qiu LW, Cao YC, Yang YQ, Yu KH (2019) Sedimentary environment and the controlling factors of organic-rich rocks in the Lucaogou Formation of the Jimusar Sag, Junggar Basin. NW China Petrol Sci 16(4):763–775. https://doi.org/10.1007/s12182-019-0353-3

Ratigan A (2016) Paleoenvironmental analysis of Cretaceous mudstones at Slope Mountain, Alaska using carbon stable isotopes. Oberlin College, 242.

Robinson SA, Hesselbo SP (2004) Fossil-wood carbon-isotope stratigraphy of the non-marine Wealden Group (Lower Cretaceous, southern England). J Geol Soc 161(1):133–145. https://doi.org/10.1144/0016-764903-004

Roddaz M, Viers J, Brusset S, Baby P, Boucayrand C, Hérail G (2006) Controls on weathering and provenance in the Amazonian foreland basin: insights from major and trace element geochemistry of Neogene Amazonian sediments. Chem Geol 226(1–2):31–65. https://doi.org/10.1016/j.chemgeo.2005.08.010

Roser BP, Korsch RJ (1986) Determination of tectonic setting of sandstone-mudstone suites using SiO_2 content and K_2O/Na_2O ratio. J Geol 94(5):635–650. https://doi.org/10.1086/629071

Rudnick RL, Gao S (2014) Composition of the continental crust. In: Holland HD, Turekian KK eds. Treatise on Geochemistry. Elsevier, pp 1–51. https://doi.org/10.1016/b978-0-08-095975-7.00301-6

Ruffell AH, Batten DJ (1990) The Barremian-Aptian arid phase in western Europe. Palaeogeogr Palaeoclimatol Palaeoecol 80(3–4):197–212. https://doi.org/10.1016/0031-0182(90)90132-Q

Ruffell A, Garden R (1997) Tectonic controls on the variation in thickness and mineralogy of pebble-beds in the Lower Greensand Group (Aptian-Albian) of the Isle of Wight, southern England. Proc Geol Assoc 108(3):215–229. https://doi.org/10.1016/S0016-7878(97)80030-2

Ruffell A, McKinley JM, Worden RH (2002) Comparison of clay mineral stratigraphy to other proxy Palaeoclimate indicators in the Mesozoic of NW Europe. Philos Trans A Math Phys Eng Sci 360(1793):675–693. https://doi.org/10.1098/rsta.2001.0961

Salazar-Jaramillo S, Fowell SJ, McCarthy PJ, Benowitz JA, Maciej GŚ, Tomsich CS (2016) Terrestrial isotopic evidence for a Middle-Maastrichtian warming event from the lower Cantwell Formation, Alaska. Palaeogeogr Palaeoclimatol Palaeoecol 441:360–376. https://doi.org/10.1016/j.palaeo.2015.09.044

Sample JC, Torres ME, Fisher A, Hong WL, Destrigneville C, Defliese WF, Tripati AE (2017) Geochemical constraints on the temperature and timing of carbonate formation and lithification in the Nankai Trough, NanTroSEIZE transect. Geochim Cosmochim Acta 198:92–114. https://doi.org/10.1016/j.gca.2016.10.013

Santos Júnior ADAD, Rossetti DDF, Murray HH (2007) Origins of the Rio Capim kaolinites (northern Brazil) revealed by $\delta^{18}O$ and δD analyses. Appl Clay Sci 37(3–4):281–294. https://doi.org/10.1016/j.clay.2007.01.005

Sauer PE, Eglinton TI, Hayes JM, Schimmelmann A, Sessions AL (2001) Compound-specific D/H ratios of lipid biomarkers from sediments as a proxy for environmental and climatic conditions. Geochim Cosmochim Acta 65(2):213–222. https://doi.org/10.1016/s0016-7037(00)00520-2

Savin SM, Lee M (1988) Isotopic studies of phyllosilicates. In: Reviews in Mineralogy and Geochemistry. 19(1):189–223.

Savin SM, Epstein S (1970) The oxygen and hydrogen isotope geochemistry of clay minerals. Geochim Cosmochim Acta 34(1):25–42. https://doi.org/10.1016/0016-7037(70)90149-3

Schwoerer P (1965) Carte de reconnaissance à l'échelle du 1/500 000. Notice explicative sur la feuille Garoua-Est. Direction des Mines et de la Géologie du Cameroun, 49

Shandini Y, Kouske PA, Nguiya S, Marcelin MP (2018) Structural setting of the Koum sedimentary basin (north Cameroon) derived from EGM2008 gravity field interpretation. Contrib Geophys Geod 48(4):281–298. https://doi.org/10.2478/congeo-2018-0013

Sheppard SMF, Gilg HA (1996) Stable isotope geochemistry of clay minerals. Clay Miner 31(1):1–24. https://doi.org/10.1180/claymin.1996.031.1.01

Silverman SR, Epstein S (1958) Carbon isotopic compositions of petroleums and other sedimentary organic materials. AAPG Bull 42:998–1012. https://doi.org/10.1306/0bda5aec-16bd-11d7-8645000102c1865d

Skelton PW, Spicer RA, Kelley SP, Gilmour I (2003) The cretaceous world. Cambridge University Press, Cambridge, UK, pp 1–360

Sofer Z (1991) Stable isotopes in petroleum exploration. In: (Merrill RK ed) Source and migration processes and evaluation techniques. pp 103–106 https://doi.org/10.1306/trhbk543c9

Spicer RA, Parrish JT (1986) Paleobotanical evidence for cool north polar climates in Middle Cretaceous (Albian-Cenomanian) time. Geology 14(8):703. https://doi.org/10.1130/0091-7613(1986)14%3c703:pefcnp%3e2.0.co;2

Sun LH, Gui HR, Chen S (2012) Geochemistry of sandstones from the Neoproterozoic Shijia formation, northern Anhui Province, China: Implications for provenance, weathering and tectonic setting. Geochemistry 72(3):253–260. https://doi.org/10.1016/j.chemer.2011.11.006

Tabor NJ, Myers TS (2015) Paleosols as indicators of paleoenvironment and paleoclimate. Annu Rev Earth Planet Sci 43(1):333–361. https://doi.org/10.1146/annurev-earth-060614-105355

Tang L, Song Y, Pang XQ, Jiang ZX, Guo YC, Zhang HA, Pan ZH, Jiang H (2020) Effects of paleo sedimentary environment in saline lacustrine basin on organic matter accumulation and preservation: A case study from the Dongpu Depression, Bohai Bay Basin. China J Petrol Sci Eng 185:106669. https://doi.org/10.1016/j.petrol.2019.106669

Tao S, Xu YB, Tang DZ, Xu H, Li S, Chen SD, Liu WB, Cui Y, Gou MF (2017) Geochemistry of the Shitoumei oil shale in the Santanghu Basin, northwest China: implications for paleoclimate conditions, weathering, provenance and tectonic setting. Int J Coal Geol 184:42–56. https://doi.org/10.1016/j.coal.2017.11.007

Tarduno JA, Brinkman DB, Renne PR, Cottrell RD, Scher H, Castillo P (1998) Evidence for extreme climatic warmth from late cretaceous arctic vertebrates. Science 282(5397):2241–2244. https://doi.org/10.1126/science.282.5397.2241

Taylor SR, McLennan SM (1985) The continental crust: Its composition and evolution. Oxford Press: Blackwell.

Taylor SR, McLennan SM (1981) The composition and evolution of the continental crust: rare earth element evidence from sedimentary rocks. Phil Trans R Soc Lond A 301(1461):381–399. https://doi.org/10.1098/rsta.1981.0119

Tchouatcha MS, Azinwi Tamfuh P, Sobdjou CK, Mbesse CO, Ngnotue T (2021) Provenance, Palaeoweathering and depositional

environment of the Cretaceous deposits from the Babouri-Figuil and Mayo Oulo-Lere basins (North-Cameroon) during the Southern Atlantic opening: Geochemical constraints. J Afr Earth Sci 174:104052. https://doi.org/10.1016/j.jafrearsci.2020.104052

Tenger Liu WH, Xu YC, Chen JF, Hu K, Gao CL (2006) Comprehensive geochemical identification of highly evolved marine hydrocarbon source rocks: organic matter, paleoenvironment and development of effective hydrocarbon source rocks. Chin J Geochem 25(4):333–340. https://doi.org/10.1007/s11631-006-0332-4

Thiry M (2000) Palaeoclimatic interpretation of clay minerals in marine deposits: an outlook from the continental origin. Earth Sci Rev 49(1–4):201–221. https://doi.org/10.1016/S0012-8252(99)00054-9

Tian Y, Zhao XM, Wang ZZ, Tu B, Xie GG, Zeng BF (2014) Geochemical characteristics and its paleoenvironmental implication of Permian Qixia Formation in Shizhu, Chongqing. Acta Petrol Sin 32:1035–1045. https://doi.org/10.14027/j.cnki.cjxb.2014.06.005

Tiwari M, Singh AK, Sinha DK (2015) Stable isotopes: tools for understanding past climatic conditions and their applications in chemostratigraphy. In: Chemostratigraphy, pp. 65–92

Tostevin R, Shields GA, Tarbuck GM, He TC, Clarkson MO, Wood RA (2016) Effective use of cerium anomalies as a redox proxy in carbonate-dominated marine settings. Chem Geol 438:146–162. https://doi.org/10.1016/j.chemgeo.2016.06.027

Tribovillard N, Algeo TJ, Lyons T, Riboulleau A (2006) Trace metals as paleoredox and paleoproductivity proxies: an update. Chem Geol 232(1–2):12–32. https://doi.org/10.1016/j.chemgeo.2006.02.012

Tyson RV, Pearson TH (1991) Modern and ancient continental shelf anoxia: an overview. Geol Soc Lond Spec Publ 58(1):1–24. https://doi.org/10.1144/gsl.sp.1991.058.01.01

van de Kamp PC, Leake BE (1985) Petrography and geochemistry of feldspathic and mafic sediments of the northeastern Pacific margin. Trans R Soc Edinb Earth Sci 76(4):411–449. https://doi.org/10.1017/s0263593300010646

Veizer J (1983) Chemical diagenesis of carbonates: Theory and application of trace element technique. In: eds Arthur MA et al. Stable isotopes in sedimentary geology. SEPM Short Course Notes 10:3.1–3.100.

Velde B (1995) Geology of clays; In: Origin and mineralogy of clays: Clays and the environment; Springer, Berlin, Heidelberg, 1–7.

Verma SP, Armstrong-Altrin JS (2013) New multi-dimensional diagrams for tectonic discrimination of siliciclastic sediments and their application to Precambrian basins. Chem Geol 355:117–133. https://doi.org/10.1016/j.chemgeo.2013.07.014

Walker GF (1975) Vermiculites. In: ed. Gieseking JE, Soil components, inorganic components. Springer Verlag, New York. 2:155–189.

Wang S, Huang XZ, Tuo J (1997) Evolutional characteristics and their paleoclimate significance of trace elements in the Hetaoyuan formation, Biyang depression. Acta Sedimentol Sin 15:65–70. https://doi.org/10.14027/j.cnki.cjxb.1997.01.012

Wang EZ, Guo TL, Li MW, Xiong L, Dong XX, Zhang NX, Wang T (2022) Depositional environment variation and organic matter accumulation mechanism of marine–continental transitional shale in the Upper Permian Longtan Formation, Sichuan Basin. SW China ACS Earth Space Chem 6(9):2199–2214. https://doi.org/10.1021/acsearthspacechem.2c00101

Weaver CE (1989) Clays, muds and shales. In: Development in sedimentology. Elsevier, Amsterdam, 44:819.

Wei WEI, Algeo TJ (2020) Elemental proxies for paleosalinity analysis of ancient shales and mudrocks. Geochimica et Cosmochimica Acta 287:341–366

Williams LB, Hervig RL, Bjørlykke K (1997) New evidence for the origin of quartz cements in hydrocarbon reservoirs revealed by oxygen isotope microanalyses. Geochim Cosmochim Acta 61(12):2529–2538. https://doi.org/10.1016/S0016-7037(97)00111-7

Worden RH, Smalley PC, Oxtoby NH (1996) The effects of thermochemical sulfate reduction upon formation water salinity and oxygen isotopes in carbonate gas reservoirs. Geochim Cosmochim Acta 60(20):3925–3931. https://doi.org/10.1016/0016-7037(96)00216-5

Wronkiewicz DJ, Condie KC (1987) Geochemistry of Archean shales from the Witwatersrand supergroup, South Africa: source-area weathering and provenance. Geochim Cosmochim Acta 51(9):2401–2416. https://doi.org/10.1016/0016-7037(87)90293-6

Wu YN, Tao S, Bi CQ, Wang ZH (2024) Geochemical characteristics of lower Cretaceous Chengzihe Formation mudstones in the Jixi Basin, China: implications for provenance, paleoenvironment and tectonic setting. ACS Earth Space Chem 8(9):1847–1866. https://doi.org/10.1021/acsearthspacechem.4c00145

Xi KL, Cao YC, Lin MR, Liu KY, Wu ST, Yuan GH, Yang T (2019) Applications of light stable isotopes (C, O, H) in the study of sandstone diagenesis: a review. Acta Geologica Sinica (Eng) 93(1):213–226. https://doi.org/10.1111/1755-6724.13769

Xie S, Nott CJ, Avsejs LA, Volders F, Maddy D, Chambers FM, Gledhill A, Carter JF, Evershed RP (2000) Palaeoclimate records in compound-specific δD values of a lipid biomarker in ombrotrophic peat. Org Geochem 31(10):1053–1057. https://doi.org/10.1016/S0146-6380(00)00116-9

Zhang K, Shields GA (2022) Sedimentary Ce anomalies: Secular change and implications for paleoenvironmental evolution. Earth Sci Rev 229:104015. https://doi.org/10.1016/j.earscirev.2022.104015

Zhang K, Liu R, Bai E, Zhao ZB, Peyrotty G, Fathy D, Chang Q, Liu ZP, Yang K, Xu C, Liu ZJ (2023) Biome responses to a hydroclimatic crisis in an Early Cretaceous (Barremian–Aptian) subtropical inland lake ecosystem. Northwest China Palaeogeogr Palaeoclimatol Palaeoecol 622:111596. https://doi.org/10.1016/j.palaeo.2023.111596

Zhao ZY, Zhao JH, Wang HJ, Liao JD, Liu CM (2007) Distribution characteristics and applications of trace elements in Junggar Basin. Nat Gas Explor Dev 30(2):30–32

Publisher's Note Springer Nature remains neutral with regard to jurisdictional claims in published maps and institutional affiliations.

Springer Nature or its licensor (e.g. a society or other partner) holds exclusive rights to this article under a publishing agreement with the author(s) or other rightsholder(s); author self-archiving of the accepted manuscript version of this article is solely governed by the terms of such publishing agreement and applicable law.